

# Actin cortex architecture regulates cell surface tension

Priyamvada Chugh<sup>1,8</sup>, Andrew G. Clark<sup>1,8,9,10</sup>, Matthew B. Smith<sup>1,8</sup>, Davide A. D. Cassani<sup>1</sup>, Kai Dierkes<sup>2,3</sup>, Anan Ragab<sup>1</sup>, Philippe P. Roux<sup>4</sup>, Guillaume Charras<sup>5,6</sup>, Guillaume Salbreux<sup>7</sup> and Ewa K. Paluch<sup>1,10</sup>

**Animal cell shape is largely determined by the cortex, a thin actin network underlying the plasma membrane in which myosin-driven stresses generate contractile tension. Tension gradients result in local contractions and drive cell deformations.** Previous cortical tension regulation studies have focused on myosin motors. Here, we show that cortical actin network architecture is equally important. First, we observe that actin cortex thickness and tension are inversely correlated during cell-cycle progression. We then show that the actin filament length regulators CFL1, CAPZB and DIAPH1 regulate mitotic cortex thickness and find that both increasing and decreasing thickness decreases tension in mitosis. This suggests that the mitotic cortex is poised close to a tension maximum. Finally, using a computational model, we identify a physical mechanism by which maximum tension is achieved at intermediate actin filament lengths. Our results indicate that actin network architecture, alongside myosin activity, is key to cell surface tension regulation.

Animal cell shape is controlled primarily by the cell cortex, a thin network of actin filaments, myosin motors and actin-binding proteins that lies directly beneath the plasma membrane<sup>1</sup>. Local changes in cortex mechanical properties, particularly in cortical tension, drive cellular deformations, such as those occurring during mitotic cell rounding, cytokinesis, migration, and tissue morphogenesis<sup>2–10</sup>. Thus, understanding cortical tension regulation is essential for understanding how cells change shape<sup>1–3</sup>.

Cortical tension is primarily generated by myosin II motors, which create contractile stresses by pulling actin filaments with respect to one another<sup>11,12</sup>. As such, myosin II function in cortical tension regulation has been studied extensively<sup>13,14</sup>. In contrast, little is known about the role of actin filament properties and organization. Models of tension generation commonly assume that actin acts as a mere scaffold, and tension is determined by myosin amounts and activity<sup>13,15–17</sup>. A recent experimental study reports that cortical actin thickness decreases as tension increases from prometaphase to metaphase and concludes that modulating myosin recruitment, rather than actin, controls cortical tension<sup>14</sup>. In contrast, recent *in vitro* studies of actomyosin networks have demonstrated that modulating actin architecture without changing myosin concentration or activity can considerably affect tension<sup>18–21</sup>. Given that actin filaments provide the substrate for myosin motors, the spatial organization of actin probably influences tension in the cortex as well. Yet, the contribution of actin network properties to cellular tension regulation remains an open question.

One major challenge to investigating the link between cortical organization and tension is that cortex thickness is below the resolution of diffraction-limited light microscopy<sup>22,23</sup>. To address this challenge, we recently developed a sub-resolution image analysis method to quantify cortex thickness and density in live cells<sup>24</sup>. Here, we use this method to investigate whether cortex thickness contributes to cortical tension regulation.

We first compared interphase and mitotic cells, as cortical tension is known to be higher in mitosis<sup>6,7,9,25–27</sup>. We found that mitotic cells have higher tension but a thinner cortex when compared with interphase cells. Using targeted genetic perturbations, we identified proteins controlling actin filament length as the main regulators of mitotic cortex thickness. Strikingly, both increasing and decreasing thickness resulted in a strong decrease in mitotic cortical tension. Finally, using a computational model, we identified a physical mechanism suggesting that, in the mitotic cortex, filament length is optimized for maximum tension generation. Together, our experiments and model show that, in addition to myosin activity, actin filament network architecture is a key regulator of contractile tension in the cell cortex.

## RESULTS

### The mitotic cortex is thinner and has higher tension than the interphase cortex

We investigated changes in actin network architecture between interphase and mitosis, as cortical tension is known to be higher

<sup>1</sup>MRC Laboratory for Molecular Cell Biology, University College London, London WC1E 6BT, UK. <sup>2</sup>Centre for Genomic Regulation, The Barcelona Institute of Science and Technology, Barcelona 08003, Spain. <sup>3</sup>Universitat Pompeu Fabra, Barcelona 08003, Spain. <sup>4</sup>Institute for Research in Immunology and Cancer, Université de Montréal, Montréal, Québec H3C 3J7, Canada. <sup>5</sup>London Centre for Nanotechnology, University College London, London WC1H 0AH, UK. <sup>6</sup>Department of Cell and Developmental Biology, University College London, London WC1E 6BT, UK. <sup>7</sup>The Francis Crick Institute, London NW1 1AT, UK. <sup>8</sup>These authors contributed equally to this work. <sup>9</sup>Present address: Institut Curie, PSL Research University, UMR144, 75005 Paris, France.

<sup>10</sup>Correspondence should be addressed to A.G.C. or E.K.P. (e-mail: [andrew.clark@curie.fr](mailto:andrew.clark@curie.fr) or [e.paluch@ucl.ac.uk](mailto:e.paluch@ucl.ac.uk))

Received 8 June 2016; accepted 4 April 2017; published online 22 May 2017; DOI: 10.1038/ncb3525

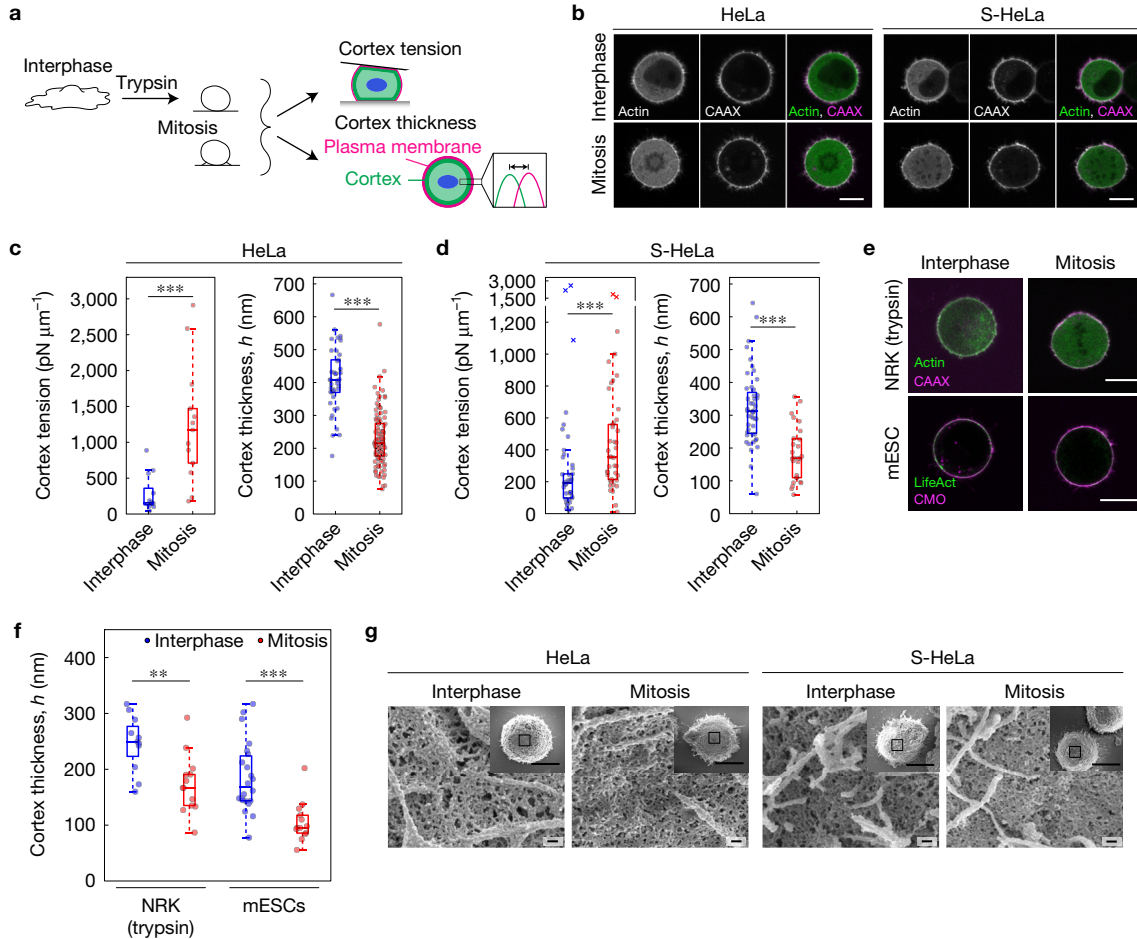


**Figure 1** The mitotic cortex is thinner and has higher tension than the interphase cortex. **(a)** Schematic representation of cortex thickness and tension measurements in adherent HeLa cells in interphase (trypsinized) and mitosis. **(b)** Adherent HeLa and S-HeLa cells synchronized in interphase (G1/S) and mitosis (prometaphase) expressing GFP-actin and mCherry-CAAX. Images are representative of 3, 13, 6 and 5 independent experiments and 41, 100, 47 and 27 cells. Scale bars, 10  $\mu\text{m}$ . **(c,d)** Box plots comparing cortex tension and cortex thickness,  $h$ , between interphase and mitotic HeLa and S-HeLa cells. Points represent individual measurements ( $n=12, 13, 41$  and 100 cells pooled across at least three independent experiments;  $P=0.0009, 1.4 \times 10^{-15}$  for adherent HeLa cells and  $n=40, 42, 47, 27$  cells (outliers included) pooled across five or six independent experiments;  $P=7.9 \times 10^{-5}, 2.4 \times 10^{-8}$  for S-HeLa cells). The points plotted with crosses were determined to be outliers (see Methods for details) and were not considered for statistical analysis. **(e)** Representative images of interphase and mitotic NRK cells (trypsinized) expressing GFP-actin and mCherry-CAAX and mESCs expressing LifeAct-GFP and labelled with plasma membrane

binding dye Cell Mask Orange (CMO). mESCs were cultured in 2i/LIF medium, where they show a rounded morphology throughout the cell cycle. Images are representative of two or three independent experiments (11, 13, 22 and 13 cells). Scale bars, 10  $\mu\text{m}$ . **(f)** Box plot comparing cortex thickness between interphase and mitotic NRK cells and mESCs. Points represent individual measurements ( $n=11, 13, 22$  and 13 cells pooled across two or three independent experiments;  $P=0.0016, 2.6 \times 10^{-5}$ ). **(g)** Scanning electron micrographs of membrane extracted cortices of adherent HeLa (left) and S-HeLa (right) cells blocked in interphase and mitosis (representative of 11–18 cells from one or two independent experiments). Scale bars, 100 nm. Insets: Lower-magnification images of whole cells; boxed areas indicate the high-magnification regions; scale bars, 10  $\mu\text{m}$ . See Supplementary Fig. 2h–j for quantifications. Welch's *t*-test *P*-values: \*\* $P < 0.01$ ; \*\*\* $P < 0.001$ . For all box plots in this figure and all subsequent figures, the box extends from the lower to upper quartile of the data, and the line denotes the median. Whiskers extend to include the most extreme values within 1.5 times the interquartile range below and above the lower and upper quartiles, respectively.

in mitosis<sup>6,9,25</sup>. We first verified the tension difference using atomic force microscopy in adherent HeLa cells synchronized in interphase and prometaphase (Fig. 1a–c and Supplementary Fig. 1). Interphase cells were detached such that they acquired a spherical morphology, comparable to that of mitotic cells (Fig. 1a,b). To rule out potential effects of cell detachment, we repeated the measurements in suspension (S)-HeLa cells, a sub-line derived from adherent HeLa cells, which show a rounded morphology throughout the cell cycle. We observed an increase in cortex tension from interphase to mitosis in both HeLa and S-HeLa cells (Fig. 1c,d).

We then asked if the cortex tension increase correlated with changes in cortex architecture. As a basic readout, we measured cortical thickness using the sub-resolution localization method we recently developed<sup>24</sup> (Fig. 1a,b). Interestingly, we found that thickness was lower in mitosis when compared with interphase in both adherent HeLa and S-HeLa cells, indicating an inverse correlation between cortex thickness and tension during the cell cycle (Fig. 1c,d). To exclude the influence of potential changes in effective membrane width on thickness measurements (Fig. 1a), we checked that the width of the plasma membrane linescan did not considerably change between interphase

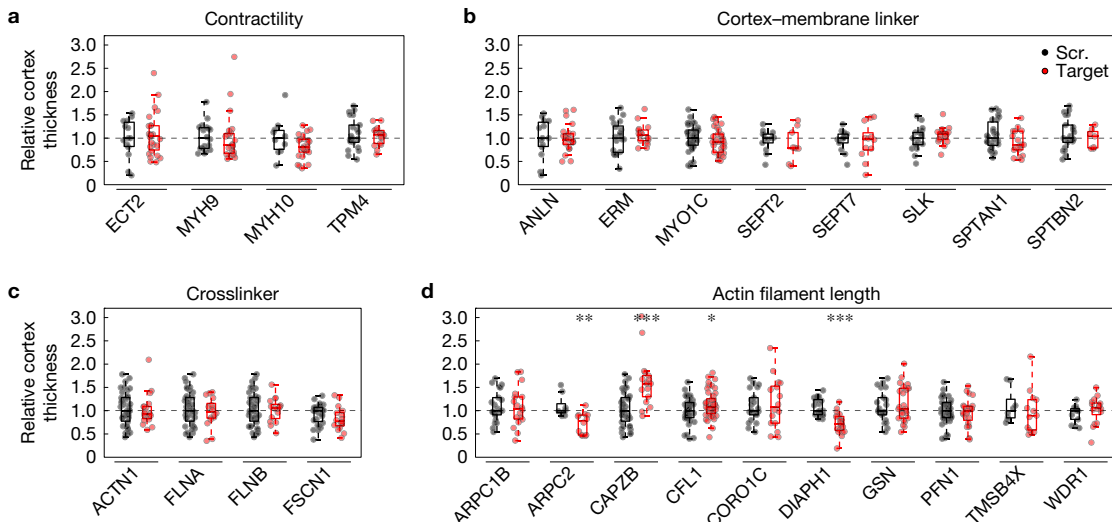


**Figure 2** Actin filament length-regulating proteins control cortex thickness in mitosis. **(a–d)** Box plots comparing relative cortex thickness in mitotic HeLa cells depleted for contractility-related ABPs **(a)**, cortex-membrane linkers **(b)**, crosslinkers **(c)** and actin filament length regulators **(d)**. Relative cortex thickness values were obtained by dividing cortex thickness in siRNA-depleted cells (Target) by the median of the corresponding scrambled control (Scr.). Points represent individual measurements ( $n=14, 26, 18, 23, 10, 25, 21, 17; 14, 24, 20, 17, 40, 33, 13, 9, 13, 12, 17, 17, 26, 17, 21, 7; 38, 18, 38, 16, 38, 16, 27, 16, 21, 18, 8, 12, 38, 17, 40, 44, 21, 16, 20, 20, 21, 25, 40, 23, 8, 13, 13$  and 16 cells pooled across two or three independent experiments;  $P=0.61, 0.86, 0.15, 0.57; 0.99, 0.47, 0.36, 0.45, 0.82, 0.35, 0.06, 0.36; 0.84, 0.48, 0.80, 0.20; 0.91, 0.0028, 0.0004, 0.034, 0.65, 3.6 \times 10^{-6}, 0.57, 0.64, 0.47$  and 0.37). Details of the siRNA treatments are given in Supplementary Table 2; depletion levels were checked by qPCR (Supplementary Fig. 4). Welch's *t*-test *P*-values: \* $P<0.05$ , \*\* $P<0.01$  and \*\*\* $P<0.001$ .

and mitosis (Supplementary Fig. 2a). Moreover, the reduced cortex thickness in mitosis could not be attributed simply to a redistribution of cortical material due to cell volume increase between interphase and mitosis<sup>28</sup> (Supplementary Fig. 2b and Supplementary Table 1). We verified that neither trypsinization, nor the method used to immobilize interphase cells, nor the treatment used for synchronization, affected cortex thickness measurements (Supplementary Fig. 2c,d). Finally, we compared cortex thickness in mitosis and interphase in detached normal rat kidney (NRK) cells, which are adherent throughout the cell cycle, and naïve mouse embryonic stem cells (mESCs), which are non-transformed and have a round morphology throughout the cell cycle (Fig. 1e). We observed a decrease in cortex thickness between interphase and mitosis in both cell lines (Fig. 1f), suggesting that mitotic cortex thinning is a widespread feature among different cell types.

We further probed cortex architecture by investigating cortex density and ultrastructure. We first quantified cortical actin density, which is an output of our thickness extraction method<sup>24</sup>, and total amounts of cortical actin (Supplementary Fig. 2e). We observed a modest but significant increase in cortex density, but no change in cortical actin amounts, from interphase to mitosis (Supplementary Fig. 2f,g). We then visualized the outer surface of the cortex in interphase and mitotic HeLa and S-HeLa cells using scanning electron microscopy (SEM) (Fig. 1g). The cortical network seemed slightly less homogenous in interphase, with a higher incidence of larger gaps; away from these gaps, network mesh size and organization in interphase and mitosis were largely comparable (Fig. 1g and Supplementary Fig. 2h-j). On the basis of these data, we concluded that changes in actin density and surface organization between interphase and mitosis were less prominent than the observed changes in cortex thickness. We thus focused on cortex thickness as a first-order readout of cortical nanoscale architecture for the remainder of the study.

7; 38, 18, 38, 16, 38, 16, 27, 16, 21, 18, 8, 12, 38, 17, 40, 44, 21, 16, 20, 20, 21, 25, 40, 23, 8, 13, 13 and 16 cells pooled across two or three independent experiments;  $P=0.61, 0.86, 0.15, 0.57; 0.99, 0.47, 0.36, 0.45, 0.82, 0.35, 0.06, 0.36; 0.84, 0.48, 0.80, 0.20; 0.91, 0.0028, 0.0004, 0.034, 0.65, 3.6 \times 10^{-6}, 0.57, 0.64, 0.47$  and 0.37). Details of the siRNA treatments are given in Supplementary Table 2; depletion levels were checked by qPCR (Supplementary Fig. 4). Welch's *t*-test *P*-values: \* $P<0.05$ , \*\* $P<0.01$  and \*\*\* $P<0.001$ .

#### Proteins controlling actin filament length regulate cortex thickness

To investigate if changes in cortex thickness could affect cortical tension directly, we searched for thickness regulators by performing a targeted short interfering RNA (siRNA) screen of key actin-binding proteins (ABPs). We explored four categories of ABPs: contractility-related proteins, cortex-membrane linkers, actin crosslinkers and actin filament length regulators. Each ABP was depleted using siRNA previously shown to reduce expression, or siRNA pools (Supplementary Table 2). The three members of the ezrin, radixin and moesin (ERM) family of actin-membrane linkers were depleted together to avoid compensation effects; we also included the kinase SLK in our targeted screen, which regulates ERM activity in mitosis<sup>29,30</sup>. To rule out compensation between the two heavy chains of myosin II, MYH9 and MYH10, we also tested the effect of the myosin inhibitor blebbistatin (Supplementary Fig. 3a). We confirmed the reduction in messenger RNA levels by quantitative real-time PCR (qPCR) (Supplementary Fig. 4 and Supplementary Table 3). We then blocked treated cells in mitosis and measured cortex thickness (Fig. 2).

Surprisingly, we found no significant effect on cortex thickness following depletion of ABPs involved in contractility generation, membrane-to-cortex attachment or actin crosslinking (Fig. 2a-c). In contrast, we found that several ABPs regulating actin assembly and disassembly, and thus actin filament length, significantly affected cortex thickness (Fig. 2d). Specifically, we found that depletion of the barbed end-capping protein CAPZB<sup>31</sup> and the actin-severing protein CFL1 (refs 32,33) led to an increase in mitotic cortex thickness, whereas depletion of the actin-nucleating and elongating formin DIAPH1 (refs 34–36) led to a thickness decrease. CFL1 knockdown and treatment with the actin filament stabilizing drug jasplakinolide were previously found to increase cortex thickness<sup>24</sup>, supporting these findings. Depletion of the ARPC2 subunit of the Arp2/3 complex also

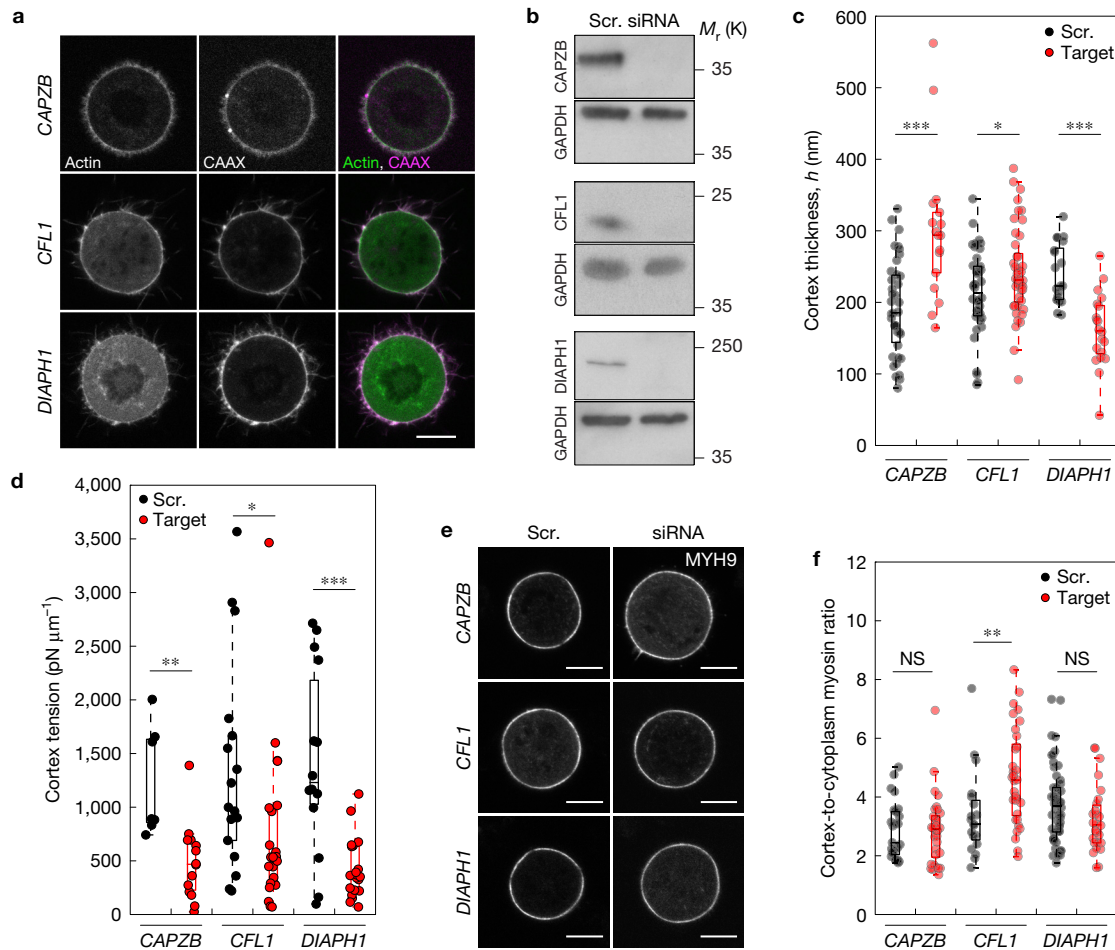


**Figure 3** Perturbation of actin filament length-regulating proteins causes a decrease in cortex thickness. **(a)** Representative images of mitotic HeLa cells expressing GFP-actin and mCherry-CAAX treated with siRNA against *CAPZB*, *CFL1* and *DIAPH1*. Images are representative of three or four independent experiments (17, 44 and 20 cells). Scale bar, 10 μm. **(b)** Western blots of *CAPZB*, *CFL1* and *DIAPH1* levels after siRNA depletion, compared with corresponding scrambled controls (Scr.). Representative blots from three independent experiments for *CAPZB* and *DIAPH1* and one experiment for *CFL1*, confirming results from ref. 24. Glyceraldehyde 3-phosphate dehydrogenase (GAPDH) was used as the loading control. Unprocessed original scans of blots are shown in Supplementary Fig. 7. **(c,d)** Box plots comparing cortex thickness (the same data are presented, normalized, in Fig. 2) and cortex tension between cells treated with Scr. siRNA or siRNA targeted against *CAPZB*, *CFL1* or *DIAPH1* (Target). Points represent

individual measurements (*n* = 38, 17, 40, 44, 20 and 20 cells pooled across three or four independent experiments, *P* = 0.0004, 0.034 and  $3.6 \times 10^{-6}$  for thickness measurements; *n* = 7, 14, 17, 24, 14 and 20 cells pooled across two to five independent experiments, *P* = 0.0046, 0.0315 and 0.0006 for tension measurements). **(e)** Representative images of mitotic HeLa cells expressing myosin IIA heavy chain MYH9-GFP, treated with siRNA against *CAPZB*, *CFL1*, *DIAPH1* and corresponding scrambled controls. Images are representative of one to three independent experiments (28, 35, 22, 28, 23 and 38 cells). Scale bars, 10 μm. **(f)** Box plots comparing the cortex-to-cytoplasm myosin ratio of MYH9-GFP for all conditions in e (*n* = 28, 35, 22, 28, 23 and 38 cells pooled across one to three independent experiments; *P* = 0.96, 0.0055 and 0.088). Welch's *t*-test *P*-values: NS *P* > 0.05, \**P* < 0.05, \*\**P* < 0.01 and \*\*\**P* < 0.001.

led to a decrease in cortex thickness. However, we did not observe any change in thickness upon depletion of ARPC1B, another Arp2/3 subunit, or following treatment with the Arp2/3 inhibitor CK-666 (Supplementary Fig. 3a). Therefore, we focused on CAPZB, CFL1 and DIAPH1 for the rest of the study. Together, our candidate knockdown approach revealed that proteins regulating actin filament length are the primary regulators of thickness of the mitotic cortex.

#### Perturbation of actin filament length-regulating proteins causes a decrease in tension

We next asked whether perturbation of the three thickness-regulating proteins identified in our screen also affected tension. Although knockdown of *CAPZB* or *CFL1* caused an increase in cortex

thickness and *DIAPH1* knockdown caused a decrease in thickness (Fig. 3a–c), cortical tension decreased in all three conditions (Fig. 3d). We also observed a decrease in average cortical stress, extracted from thickness and tension, in all three knockdown conditions (Supplementary Table 4). Furthermore, stabilization of actin filaments with jasplakinolide, which increases cortical thickness<sup>24</sup>, also led to a tension decrease in mitotic cells (Supplementary Fig. 3b). Together, these data indicate that the relationship between tension and thickness during mitosis is non-monotonic, and treatments leading to either an increase or decrease in cortex thickness result in lower tension.

We verified that thickness changes following knockdown of *CAPZB*, *CFL1* or *DIAPH1* were not due to changes in effective plasma

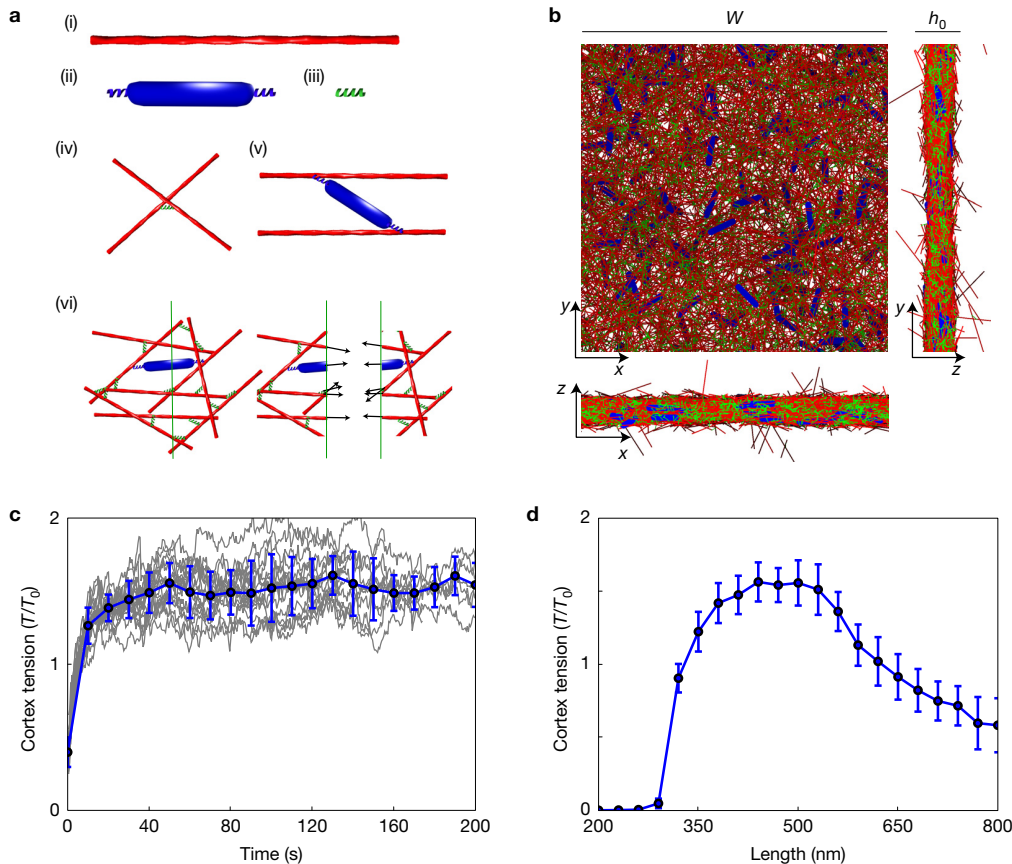


**Figure 4** A computational model of cortex tension generation predicts maximal tension at intermediate actin filament lengths. (a) Components of the simulation: (i) actin filament, (ii) myosin minifilament, (iii) crosslinker, (iv) example of crosslinked actin filaments, (v) example of a myosin motor binding two actin filaments, (vi) tension measurement by slicing the network; arrows represent forces within the network components. (b) Projections of an initialized simulation from the top (xy) and the sides (xz, yz).  $W$ , width of simulation box;  $h_0$ , seeding thickness. (c) Plot of tension ( $T/T_0$ ) as a function of time for an ensemble of simulations with filament length of 500 nm (see Supplementary Table 5 for the other parameters). Grey

membrane width or cell size (Supplementary Fig. 3c–e). We then checked for possible changes in cortex density and amounts. We found that cortex density was unchanged in *CAPZB* and *CFL1* knockdown cells but slightly increased upon *CFL1* depletion (Supplementary Fig. 3f), whereas total cortical actin amounts followed the same pattern as cortex thickness (Supplementary Fig. 3g).

Previous studies have focused on myosin activity as the primary determinant of cortical tension. We thus investigated levels of total and phosphorylated myosin in the different conditions. We observed a slight increase in myosin regulatory light chain (MRLC) expression following *CAPZB* and *DIAPH1* knockdown, but no substantial change in phosphorylated MRLC levels following any of the knockdowns (Supplementary Fig. 3h,i). We then investigated myosin localization using HeLa cells expressing myosin IIA heavy chain (MYH9) fused to green fluorescent protein (GFP). The cortex-to-cytoplasm ratio of MYH9-GFP intensity was unchanged following *CAPZB* and *DIAPH1* depletion, and even slightly higher following *CFL1* knockdown (Fig. 3e,f). Together, our results suggest that modulating cortex thickness by actin filament length regulators decreases mitotic cortex

lines represent measurements for a single plane in a simulation; blue dots are mean values ( $\pm$  s.d.) for each time point;  $n=9$  simulations; tension is measured along two planes in each simulation. The magnitude at which tension saturates in the simulations is comparable to experimental tension values with our choice of myosin stall force (see Discussion of Model Assumptions in the Supplementary Note). (d) Plot of cortex tension as a function of actin filament length. Blue dots represent mean tension values after 25 s ( $\pm$  s.d.) calculated from nine simulations. In c and d, tension is normalized to  $T_0 = 230 \text{ pN } \mu\text{m}^{-1}$  (see Supplementary Note for details).

tension, and that this tension change does not result from a decrease in myosin II levels or localization at the cortex.

#### A computational model predicts maximum cortex tension at intermediate actin filament lengths

To investigate how changes in actin filament length could affect cortex tension, we developed a computational model of the actin cortex. The components of the model are actin filaments, myosin minifilaments and crosslinkers (Fig. 4ai–iii and Supplementary Fig. 5a and Supplementary Table 5). For simplicity, actin filaments are described as rigid rods (see Supplementary Note for details). Filaments are bound to one another by passive crosslinkers with finite length that behave as linear springs (Fig. 4aiiv). Myosin minifilaments are represented as rigid rods that can bind to actin filaments and walk towards their plus ends (Fig. 4av). Resistance to motor walking is described by an effective friction (Supplementary Table 5). Filament centre-of-mass positions are chosen randomly within a box of equal length and width  $W$  and initial seeding thickness  $h_0$  (Fig. 4b and Supplementary Fig. 5b; see Supplementary Note for details).

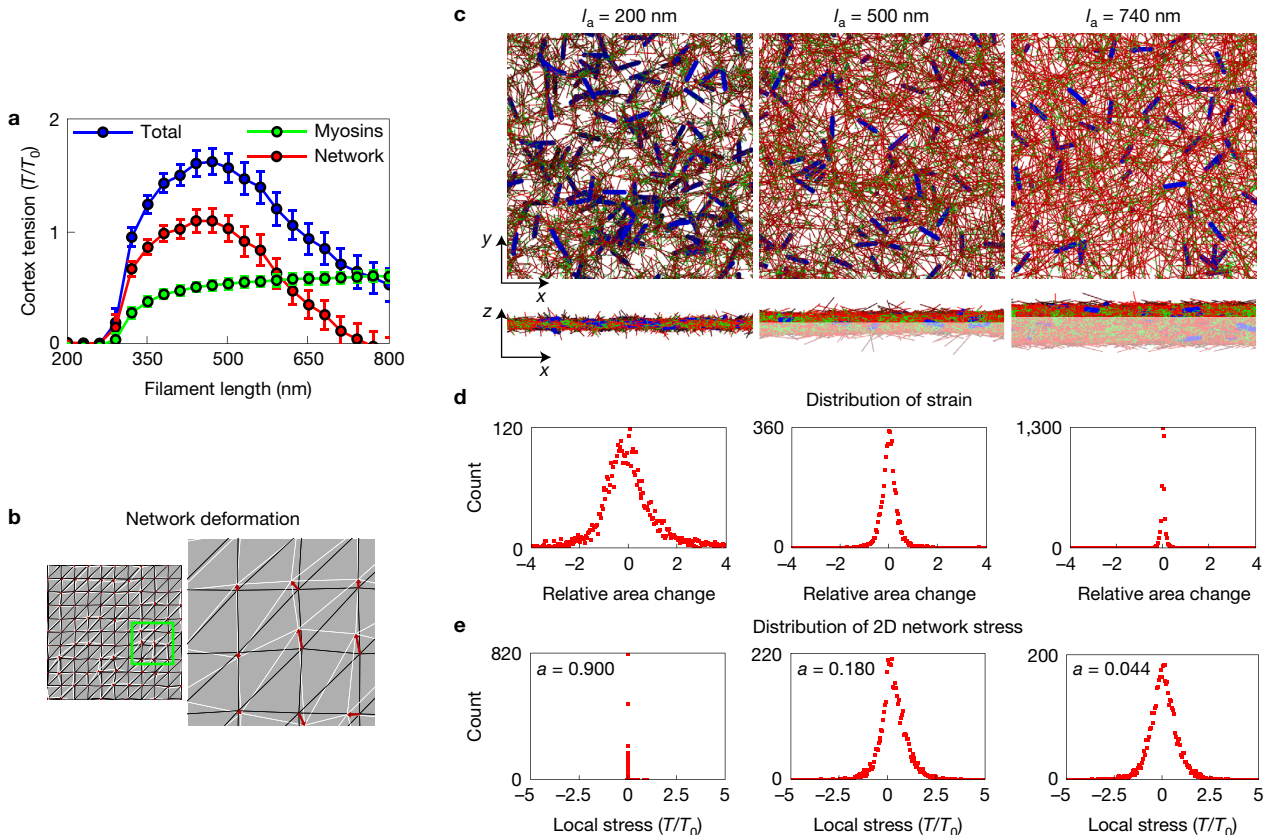


**Figure 5** Local network behaviour in response to myosin-induced stresses. **(a)** Plot of cortex tension as a function of actin filament length separating the total tension into the tension exerted within myosin motors and the network tension exerted within actin filaments and crosslinkers. Dots represent mean tension values after 25 s ( $\pm$ s.d.) calculated from nine simulations. **(b)** Example of triangulation used for measuring strain in the network. The black lines are triangles before network deformation; white lines are triangles after deformation; red arrows are the displacement field. The green box marks the zoomed inset (right). **(c)** Projections of simulated cortical networks with different actin filament lengths ( $I_a$ ). xy and xz projections were generated after 100 s of simulation runs. The whitened section of the network in the xz view is not

To investigate cortical tension generation, we simulated networks of filaments in three dimensions with periodic boundary conditions along the  $x$  and  $y$  dimensions and free boundary conditions along the  $z$  direction (Fig. 4b and Supplementary Fig. 5b). We then measured the tension exerted in the network in transversal cross-sections over time (Fig. 4avi,c and Supplementary Fig. 5c,d). We found that, after transient network reorganization ( $\sim 20$  s), tension seemed to fluctuate around a steady-state value (Fig. 4c).

We then tested how cortical tension varies with actin filament length (Supplementary Videos 1–3). The seeding thickness,  $h_0$ , was taken to be proportional to filament length, whereas the actin density and number of myosin motors in the cortex were kept constant, as suggested by our experiments (Supplementary Fig. 3f,h,i and Fig. 3e,f). We found that tension strongly varied with filament length, with a tension maximum at intermediate lengths (Fig. 4d).

We tested the robustness of our results to variability in filament length, and found that various Gaussian distributions in length did not affect our conclusions (Supplementary Fig. 5e). To test whether

shown in the xy view. **(d,e)** Local strain and local 2D network stress distributions in the deformed networks for filament lengths of 200 nm (left), 500 nm (middle) and 740 nm (right) (see Supplementary Note for a description of strain calculation). **(d)** Positive strain corresponds to stretched regions, negative strain to compressed regions. The strain distributions are largely symmetric, and shorter-filament networks exhibit higher strain than networks with longer filaments. **(e)** Network stress distributions are asymmetric, with larger positive stresses. Stress asymmetry is more pronounced for shorter-filament networks. Distribution asymmetry is quantified with the parameter  $a = (T_+ - T_-)/(T_+ + T_-)$ , with  $T_+$  and  $T_-$  the sums of positive and negative local stresses. Tensions are normalized to  $T_0 = 230 \text{ pN } \mu\text{m}^{-1}$ .

changing thickness could affect cortex tension independently of filament length, we carried out simulations with varying seeding thickness but fixed cortex density, filament length and number of motors. We found that, whereas thin networks ( $< 200$  nm) produced slightly lower tension, for thicker networks tension changed very little with seeding thickness, and no maximum was observed (Supplementary Fig. 5f). This suggests that filament length, and not simply seeding thickness, influences tension in our simulations. Finally, we carried out simulations with varying filament length, but fixed seeding thickness, actin density and thus total cortical actin amount. We found that maximal tension was obtained for intermediate filament lengths (Supplementary Fig. 5g). Together, these results indicate that changing actin filament length can modulate cortical tension and that the non-monotonic tension–filament length relationship is not dependent on changes in the total amount of cortical material.

We next investigated the physical mechanism underlying the tension maximum at intermediate filament lengths. To this end, we examined tension acting within myosin motors, and tension acting

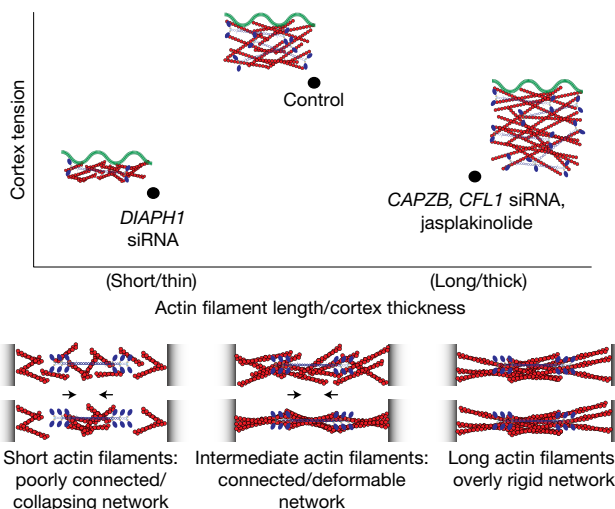


**Figure 6** Actin cortex architecture regulates cortical tension. Our experimental measurements and simulations indicate that cortical tension is maximum at intermediate actin filament length and intermediate cortex thickness (top panel). Conditions that either increase or decrease cortex thickness/actin filament length result in lower tension in mitotic cells. Our simulations suggest a physical mechanism for this non-monotonic relationship (bottom panel). Whereas networks of short filaments are too poorly connected to allow for build-up of myosin-induced stresses, networks of long filaments are too rigid to allow for sufficiently asymmetric stress generation. At intermediate filament lengths, networks are sufficiently connected for tension generation, and sufficiently compliant to promote stress asymmetry and the build-up of positive tensile stresses, leading to an overall high contractile tension.

within the actin and crosslinker network (Fig. 5a). We observed that, whereas tension within myosins increases with actin filament length and eventually saturates, tension in the actin network exhibits a maximum as a function of filament length. This indicates that the non-monotonic tension–filament length relationship arises from the response of the actin network to myosin-induced stresses. We thus analysed the behaviour of the actin network in our simulations. We calculated local isotropic strain and two-dimensional (2D) network stress for short (200 nm), intermediate (500 nm) and long (740 nm) actin filaments (Fig. 5b,c). We found that strain distributions have as many stretched as compressed regions, as expected in a non-deformable simulation box (Fig. 5d). The network shows higher strain for shorter filaments, indicating that short-filament networks are more compliant (Fig. 5d). In contrast, stress distributions are asymmetric, with more regions under positive (tensile) stress than negative (compressive) stress, resulting in networks under overall contractile tension (Fig. 5e). This 2D stress asymmetry is higher for shorter filaments, suggesting that larger local network deformation promotes stress asymmetry (Fig. 5e).

To generate high tension, actin networks must first be dense and connected enough and second show an asymmetry in stress favouring positive stress build-up. In the short-filament case, the network has high stress asymmetry, but seems not connected enough for stress generation at the network level. In the long-filament case, myosins generate high tension, but stress asymmetry is low, presumably because of high network rigidity, resulting in low overall tension. At intermediate filament length, myosins generate sufficient tension and stress asymmetry is high, resulting in contractile tension build-up. Together, this results in maximum tension at intermediate filament lengths.

Our simulations provide a physical mechanism that could account for our experimental observations (Fig. 3), and suggest that cortical actin filaments in mitosis are close to an optimal, intermediate filament length for maximal tension generation (Fig. 6). More generally, our model identifies a mechanism by which cortical tension can be modulated independently of changes in myosin motor density and activity, by fine-tuning actin filament structural properties.

## DISCUSSION

We asked here whether changing the nanoscale architecture of the cortical actin network could modulate cell surface tension independently of myosin activity. To investigate the effect of cortex thickness, a first-level readout of cortex architecture, on cortical tension, we used a targeted RNA interference screen to find thickness regulators. Interestingly, only a few of the proteins tested strongly affected cortical thickness. Functional redundancy may have masked the effects of some of the proteins tested. Nonetheless, neither depletion of myosin II heavy chains (MYH9 and MYH10), nor inhibition of myosin II activity with blebbistatin, significantly affected cortex thickness (Fig. 2a and Supplementary Fig. 3a). This suggests that myosin II, a likely candidate for thickness regulation as contractility could lead to cortex compaction by aligning actin filaments, has no effect on cortical thickness. Furthermore, neither depletion of the three ERM family proteins together nor depletion of their mitotic regulator SLK had any significant effect on thickness (Fig. 2b). This suggests that membrane-to-cortex attachment, which is strongly modulated by ERM proteins<sup>37,38</sup>, is not a regulator of cortical thickness.

All of the hits identified in our targeted screen are actin filament length regulators. No method is currently available to directly measure filament length in the cellular cortex. However, both cofilin and capping protein reduce filament length *in vitro*<sup>32,39,40</sup>, and DIAPH1 not only nucleates but also elongates actin filaments<sup>41</sup>. Recent work indicates that capping protein and formins can even form a complex at filament ends to precisely regulate filament length<sup>40</sup>. These studies suggest that these proteins should affect cortical actin filament length in the same way.

Both increasing and decreasing cortex thickness led to a strong tension decrease in mitotic cells. To explore physical mechanisms that could account for these observations, we developed a computational model of the contractile cortex. The model builds on previous work on tension generation in 2D networks<sup>42,43</sup> and expands them to investigate the influence of actin organization in 3D. For simplicity, we did not incorporate steric interactions, explicit diffusion, filament bending or turnover (Supplementary Note). Our simplified model nonetheless indicates that, at fixed myosin levels, maximum tension is generated for intermediate actin filament lengths under a large range of conditions (Supplementary Fig. 5e–g). The non-monotonic tension–filament length relationship seems to arise from an asymmetry in actin network response to myosin forces, which generate more tensile (positive) than compressive (negative) stresses (Figs 5 and 6). This effect is maximal at intermediate filament lengths, where the network is both sufficiently connected, which is required for stress generation by myosins, and sufficiently compliant, which promotes stress asymmetry. A similar behaviour at the level of individual filaments, which can buckle under compression, thus relaxing negative stresses while accumulating positive stresses, has been proposed previously to account

for positive tension build-up in isotropic networks<sup>19,44,45</sup>. Interestingly, in our simulations asymmetric stress generation is achieved without introducing filament bending. It will be interesting to investigate the combined effect of filament bending and the asymmetric network response shown by our simulations.

Tension regulation by fine-tuning filament length could provide a flexible way to modulate tension, as it can be achieved rapidly and by a multitude of different mechanisms. The cortex thinning between interphase and mitosis (Fig. 1) could result from filament shortening. However, the three hits identified in our mitotic thickness screen do not seem to directly control this cortex thinning (Supplementary Fig. 6). Given the complexity of the cellular changes at mitosis entry, many players probably act in a coordinated manner to effect the concomitant actin architecture remodelling. Surprisingly, Ect2, a key cortex regulator at the interphase–mitosis transition<sup>27</sup>, does not seem to regulate cortex thickness (Fig. 2a). It is possible that Ect2 mainly modulates myosin activity, whereas other proteins affect actin organization. Elucidating how exactly cortex architecture is controlled during this transition will be an important question for future studies.

Myosins have been commonly assumed to be the primary regulators of cortical tension<sup>13–15</sup>. Our study identifies actin filament length as an additional key regulator. Importantly, the tension decrease upon depletion of filament length regulators is comparable to the tension decrease upon myosin II inhibition (Fig. 3d and Supplementary Fig. 3b). Thus, modulating actin filaments and myosin activity could play equally important roles in tension regulation. A recent *in vitro* study shows that the degree of network connectivity modulates actomyosin contractility<sup>18</sup>. This is consistent with our model, as increasing filament length effectively increases the crosslinking level, and thus network connectivity. However, redundancy between the multiple cortical crosslinkers<sup>46</sup> and the fact that myosin itself acts as a crosslinker<sup>47</sup> make the direct study of crosslinker influence on tension more difficult in cells than *in vitro*. Nonetheless, crosslinking could provide yet another level of tension regulation.

Together, our study highlights that cortical tension, and the resulting cellular surface tension, are not controlled by myosin II activity alone and can be regulated at multiple levels. Future studies will be required to dissect the relative contributions of different mechanisms of tension regulation during specific tension-driven cellular shape changes. □

## METHODS

Methods, including statements of data availability and any associated accession codes and references, are available in the online version of this paper.

*Note: Supplementary Information is available in the online version of the paper*

## ACKNOWLEDGEMENTS

We thank B. Baum, K. Chalut, A. Jégou, G. Romet-Lemonne and members of the Paluch laboratory, particularly A. Chaigne, M. Serres and B. A. Truong Quang, for discussions and comments on the manuscript. We thank A. Yonis and M. Turmaine for technical help with SEM, R. Henriques for advice on AFM analysis, C. Verstreken (K. Chalut lab) for preparing the mESC cells used for cortex thickness measurements and the MRC-LMBC imaging facility for technical support. We acknowledge support from the Medical Research Council UK (MRC programme award MC\_UU\_12018/5), the Human Frontier Science Program (Young Investigator Grant to G.C., P.P.R. and E.K.P.), the European Research Council (starting grant 311637-MorphoCorDiv to E.K.P.) and the Polish Ministry of Science and Higher Education (grant 454/N-MPG/2009/0 to E.K.P.). We also acknowledge

the International Institute of Molecular and Cell Biology in Warsaw, the Max Planck Society and the Canadian Institutes of Health Research (CIHR Grant MOP123408 to P.P.R.). K.D. has received funding from the Spanish Ministry of Economy and Competitiveness, Plan Nacional, BFU2010-16546 and Centro de Excelencia Severo Ochoa 2013–2017, SEV-2012-0208, as well as the CERCA Programme/Generalitat de Catalunya. P.P.R. holds a Canada Research Chair in Cell Signaling and Proteomics, and a Chercheur-boursier senior award from the Fonds de Recherche Santé Québec (FRQS). G.S. is supported by the Francis Crick Institute, which receives its core funding from Cancer Research UK (FC001317), the UK Medical Research Council (FC001317) and the Wellcome Trust (FC001317).

## AUTHOR CONTRIBUTIONS

P.C., A.G.C., M.B.S., G.S. and E.K.P. designed the research and wrote the paper; P.C. carried out most of the experiments and image analysis; A.G.C. carried out some cortical thickness measurements and developed analysis tools; P.C. and A.G.C. designed the experiments and analysed the data; D.A.D.C. carried out the AFM experiments; K.D. designed the image analysis and linescan extraction software; A.R. carried out the myosin western blot experiments; M.B.S. and G.S. designed the computational model; M.B.S. carried out simulations and wrote the SEM picture analysis plugin; G.C. and P.P.R. provided technical support and conceptual advice. All authors discussed the results and manuscript.

## COMPETING FINANCIAL INTERESTS

The authors declare no competing financial interests.

Published online at <http://dx.doi.org/10.1038/ncb3525>

Reprints and permissions information is available online at [www.nature.com/reprints](http://www.nature.com/reprints)  
Publisher's note: Springer Nature remains neutral with regard to jurisdictional claims in published maps and institutional affiliations.

1. Salbreux, G., Charras, G. & Paluch, E. Actin cortex mechanics and cellular morphogenesis. *Trends Cell Biol.* **22**, 536–545 (2012).
2. Bray, D. & White, J. G. Cortical flow in animal cells. *Science* **239**, 883–888 (1988).
3. Clark, A. G. & Paluch, E. in *Cell Cycle in Development* Vol. 1 (ed. Kubiak, J. Z.) 31–73 (Springer, 2011).
4. Heisenberg, C. P. & Bellaïche, Y. Forces in tissue morphogenesis and patterning. *Cell* **153**, 948–962 (2013).
5. Levayer, R. & Lecuit, T. Biomechanical regulation of contractility: spatial control and dynamics. *Trends Cell Biol.* **22**, 61–81 (2012).
6. Maddox, A. S. & Burridge, K. RhoA is required for cortical retraction and rigidity during mitotic cell rounding. *J. Cell Biol.* **160**, 255–265 (2003).
7. Matzke, R., Jacobson, K. & Radmacher, M. Direct, high-resolution measurement of furrow stiffening during division of adherent cells. *Nat. Cell Biol.* **3**, 607–610 (2001).
8. Sedzinski, J. et al. Polar actomyosin contractility destabilizes the position of the cytokinetic furrow. *Nature* **476**, 462–466 (2011).
9. Stewart, M. P. et al. Hydrostatic pressure and the actomyosin cortex drive mitotic cell rounding. *Nature* **469**, 226–230 (2011).
10. Bergert, M. et al. Force transmission during adhesion-independent migration. *Nat. Cell Biol.* **17**, 524–529 (2015).
11. Vicente-Manzanares, M., Ma, X., Adelstein, R. S. & Horwitz, A. R. Non-muscle myosin II takes centre stage in cell adhesion and migration. *Nat. Rev. Mol. Cell Biol.* **10**, 778–790 (2009).
12. Clark, A. G., Wartlick, O., Salbreux, G. & Paluch, E. K. Stresses at the cell surface during animal cell morphogenesis. *Curr. Biol.* **24**, R484–R494 (2014).
13. Tinevez, J.-Y. et al. Role of cortical tension in bleb growth. *Proc. Natl. Acad. Sci. USA* **106**, 18581–18586 (2009).
14. Ramanathan, S. P. et al. Cdk1-dependent mitotic enrichment of cortical myosin II promotes cell rounding against confinement. *Nat. Cell Biol.* **17**, 148–159 (2015).
15. Mayer, M., Depken, M., Bois, J. S., Julicher, F. & Grill, S. W. Anisotropies in cortical tension reveal the physical basis of polarizing cortical flows. *Nature* **467**, 617–621 (2010).
16. Turlier, H., Audoly, B., Prost, J. & Joanny, J. F. Furrow constriction in animal cell cytokinesis. *Biophys. J.* **106**, 114–123 (2014).
17. Salbreux, G., Joanny, J. F., Prost, J. & Pullarkat, P. Shape oscillations of non-adhering fibroblast cells. *Phys. Biol.* **4**, 268–284 (2007).
18. Ennoman, H. et al. Architecture and connectivity govern actin network contractility. *Curr. Biol.* **26**, 616–626 (2016).
19. Murrell, M. P. & Gardel, M. L. F-actin buckling coordinates contractility and severing in a biometric actomyosin cortex. *Proc. Natl. Acad. Sci. USA* **109**, 20820–20825 (2012).
20. Reymann, A.-C. et al. Actin network architecture can determine myosin motor activity. *Science* **336**, 1310–1314 (2012).
21. Alvarado, J., Sheinman, M., Sharma, A., MacKintosh, F. C. & Koenderink, G. H. Molecular motors robustly drive active gels to a critically connected state. *Nat. Phys.* **9**, 591–597 (2013).
22. Hanakam, F., Albrecht, R., Eckerskorn, C., Matzner, M. & Gerisch, G. Myristoylated and non-myristoylated forms of the pH sensor protein hisactophilin II: intracellular shuttling to plasma membrane and nucleus monitored in real time by a fusion with green fluorescent protein. *EMBO J.* **15**, 2935–2943 (1996).

23. Charras, G. T., Hu, C.-K., Coughlin, M. & Mitchison, T. J. Reassembly of contractile actin cortex in cell blebs. *J. Cell Biol.* **175**, 477–490 (2006).
24. Clark, A. G., Dierkes, K. & Paluch, E. K. Monitoring actin cortex thickness in live cells. *Biophys. J.* **105**, 570–580 (2013).
25. Fischer-Friedrich, E., Hyman, A. A., Jülicher, F., Müller, D. J. & Helenius, J. Quantification of surface tension and internal pressure generated by single mitotic cells. *Sci. Rep.* **4**, 6213 (2014).
26. Kunda, P., Pelling, A. E., Liu, T. & Baum, B. Moesin controls cortical rigidity, cell rounding, and spindle morphogenesis during mitosis. *Curr. Biol.* **18**, 91–101 (2008).
27. Matthews, H. K. *et al.* Changes in ect2 localization couple actomyosin-dependent cell shape changes to mitotic progression. *Dev. Cell* **23**, 371–383 (2012).
28. Zlotek-Zlotkiewicz, E., Monnier, S., Cappello, G., Le Berre, M. & Piel, M. Optical volume and mass measurements show that mammalian cells swell during mitosis. *J. Cell Biol.* **211**, 765–774 (2015).
29. Carreno, S. *et al.* Moesin and its activating kinase Slik are required for cortical stability and microtubule organization in mitotic cells. *J. Cell Biol.* **180**, 739–746 (2008).
30. Machicoane, M. *et al.* SLK-dependent activation of ERMs controls LGN-NuMA localization and spindle orientation. *J. Cell Biol.* **205**, 791–799 (2014).
31. Cooper, J. A. & Sept, D. New insights into mechanism and regulation of actin capping protein. *Int. Rev. Cell Mol. Biol.* **267**, 183–206 (2008).
32. Carlier, M. F. *et al.* Actin depolymerizing factor (ADF/cofilin) enhances the rate of filament turnover: implication in actin-based motility. *J. Cell Biol.* **136**, 1307–1322 (1997).
33. Bamburg, J. R. Proteins of the ADF/cofilin family: essential regulators of actin dynamics. *Annu. Rev. Cell Dev. Biol.* **15**, 185–230 (1999).
34. Bovellan, M. *et al.* Cellular control of cortical actin nucleation. *Curr. Biol.* **24**, 1628–1635 (2014).
35. Rosa, A., Vlassaks, E., Pichaud, F. & Baum, B. Ect2/Pbl acts via Rho and polarity proteins to direct the assembly of an isotropic actomyosin cortex upon mitotic entry. *Dev. Cell* **32**, 604–616 (2015).
36. Campellone, K. G. & Welch, M. D. A nucleator arms race: cellular control of actin assembly. *Nat. Rev. Mol. Cell Biol.* **11**, 237–251 (2010).
37. Diz-Munoz, A. *et al.* Control of directed cell migration *in vivo* by membrane-to-cortex attachment. *PLoS Biol.* **8**, e1000544 (2010).
38. Rouven Bruckner, B., Pietuch, A., Nehls, S., Rother, J. & Janshoff, A. Ezrin is a major regulator of membrane tension in epithelial cells. *Sci. Rep.* **5**, 14700 (2015).
39. Kim, T., Cooper, J. A. & Sept, D. The interaction of capping protein with the barbed end of the actin filament. *J. Mol. Biol.* **404**, 794–802 (2010).
40. Bombardier, J. P. *et al.* Single-molecule visualization of a formin-capping protein ‘decision complex’ at the actin filament barbed end. *Nat. Commun.* **6**, 8707 (2015).
41. Kovar, D. R., Harris, E. S., Mahaffy, R., Higgs, H. N. & Pollard, T. D. Control of the assembly of ATP- and ADP-actin by formins and profilin. *Cell* **124**, 423–435 (2006).
42. Hiraiwa, T. & Salbreux, G. Role of turnover in active stress generation in a filament network. *Phys. Rev. Lett.* **116**, 188101 (2016).
43. Dasanayake, N. L., Michalski, P. J. & Carlsson, A. E. General mechanism of actomyosin contractility. *Phys. Rev. Lett.* **107**, 118101 (2011).
44. Lenz, M., Thoresen, T., Gardel, M. L. & Dinner, A. R. Contractile units in disordered actomyosin bundles arise from F-actin buckling. *Phys. Rev. Lett.* **108**, 238107 (2012).
45. Soares e Silva, M. *et al.* Active multistage coarsening of actin networks driven by myosin motors. *Proc. Natl. Acad. Sci. USA* **108**, 9408–9413 (2011).
46. Biro, M. *et al.* Cell cortex composition and homeostasis resolved by integrating proteomics and quantitative imaging. *Cytoskeleton* **70**, 741–754 (2013).
47. Stam, S., Alberts, J., Gardel, M. L. & Munro, E. Isoforms confer characteristic force generation and mechanosensation by myosin II filaments. *Biophys. J.* **108**, 1997–2006 (2015).

## METHODS

**Cell culture, plasmids and experimental treatments.** Wild-type HeLa cells were a gift from the MPI-CBG Technology Development Studio (TDS). The S-HeLa line was derived from HeLa TDS by constant culturing on low-adherent flasks (catalogue no. 3815, Corning). NRK cells were a gift from the laboratory of Mark Marsh (MRC-LMBC, University College London). Adherent HeLa, S-HeLa and NRK cells were cultured in DMEM (Gibco, Invitrogen/Life Technologies) supplemented with 10% heat-inactivated fetal bovine serum (Gibco), 100 U ml<sup>-1</sup> penicillin, 100 µg ml<sup>-1</sup> streptomycin and 2 mM L-glutamine at 37 °C with 5% CO<sub>2</sub>. The Lifeact mESCs were provided by the laboratory of Kevin Chalut (Wellcome Trust/Medical Research Council Cambridge Stem Cell Institute). mESCs were cultured on 0.1% gelatin at all times in 2i-LIF medium, as described in ref. 48, which is N2B27 medium (Invitrogen) supplemented with MEK inhibitor (1 µM PD0325901), GSK3 inhibitor (3 µM CHIR99021) and leukaemia inhibitory factor (LIF). None of the cell lines used in this study were found in the database of commonly misidentified cell lines maintained by ICLAC and NCBI Biosample. mESCs were tested for mycoplasma contamination; other cell lines used in this study were not authenticated and were not tested for mycoplasma contamination.

eGFP-CAAX was a gift from John Carroll (Monash University, Australia). eGFP was replaced with mCherry by restriction digest by Martin Bergert (MRC-LMBC, University College London) to create the mCherry-CAAX fusion. The GFP-actin construct was obtained by cloning human beta-actin into pcGFP-C2 (Clontech, Takara Bio Europe). Jasplakinolide (Invitrogen/Life Technologies) was added to final concentrations of 20 nM. Blebbistatin (±) (Tocris Biosystems) and CK-666 (Merck Millipore) were both used at a final concentration of 100 µM. All drug treatments were carried out for ~20 min–1 h before imaging and equivalent volumes of DMSO were used as controls.

**Cell-cycle synchronization and preparation for microscopy.** Cells were synchronized in interphase (G1/S-phase) by single thymidine block. The block was carried out by incubating cells overnight (~16–24 h) in 2 mM thymidine. For measurements in adherent cells, cells were detached from the dish using trypsin–EDTA (catalogue no. 25300-054, Life Technologies) and immobilized for imaging by either confining the cells in 25 µm wide polydimethylsiloxane channels (prepared as described in ref. 10) or by brief centrifugation on poly-L-lysine-coated 35 mm glass-bottom dishes (WillCo Wells HBST-3522). For enzyme-free detachment of interphase cells, Cell Dissociation Buffer, enzyme-free (catalogue no. 13151-014, Thermo Fisher Scientific) was used. To enrich cells in mitosis (prometaphase), the cells were treated with 2 µM S-trityl-L-cysteine (STLC)<sup>49</sup> for 5–7 h before imaging. For electron microscopy and tension-measurement experiments, the STLC treatments were carried out overnight.

**Transfection.** Cells were plated on 35 mm glass-bottom imaging dishes (WillCo Wells HBST-3522) at least 16 h before transfection. For plasmids, 0.3–0.5 µg DNA was transfected by lipofection (Lipofectamine 2000, catalogue no. 11668-027, Life Technologies) according to manufacturer's instructions. siRNAs were transfected using Lipofectamine RNAiMax (Invitrogen, Life Technologies) for specified treatment times (Supplementary Table 2). Detailed information about siRNA treatments is given in Supplementary Table 2.

**Confocal microscopy imaging and cortex thickness measurements.** For all live cortex thickness measurements, two-colour image stacks (30–70 z slices, 100 nm intervals) were acquired around the equatorial plane of rounded cells using a ×60 colour-corrected objective (1.40 numerical aperture OSC2 PlanApoN) mounted on an Olympus FV1200 microscope. For chromatic correction 200 nm diameter multicolour TetraSpeck beads (Invitrogen) were imaged using the same settings as used for the cells. After correcting for the chromatic shift in x, y and z, and magnification using custom software written in MATLAB, a single equatorial plane was selected for each image using Fiji image analysis software<sup>50</sup>. Cortex thickness and density were then extracted using the protocol detailed in ref. 24; the custom software for image analysis and linescan extraction is available publicly (details in 'Code availability' section later). For membrane width measurements, we measured the full-width at half-maximum of the plasma membrane intensity peak by interpolating the x position on the linescan on either side of the peak by linear interpolation of the two closest points. The half-maximum was defined as half the difference between the peak intensity and intracellular background. Cell radius measurements were made by fitting the cell segmentation used for thickness analysis to a circle.

**Western blotting.** For western blotting, cells were centrifuged at 1,000g for 3 min. The pellet was washed with PBS and then lysed using RIPA lysis buffer (Santa Cruz Biotechnology). The lysates were clarified by centrifugation at 8,000g for 4 min at 4 °C, diluted 1:1 with ×2 Laemmli buffer (Sigma-Aldrich), incubated for 5 min at 95 °C and loaded onto NuPage 4–12% Bis–Tris gradient gels (Invitrogen/Life Technologies). Primary antibodies used were 1:500 anti-DIAPH1

(catalogue no. 96784, Abcam), 1:1,000 anti-CAPZB (AB6017, Millipore), 1:1,000 anti-CFL1 (3318S, Cell Signaling), 1:100,000 anti-GAPDH (1D4, NB300-221, Novus Biologicals). Myosin amount and activity were assessed by running whole cell lysates on NuPage 14% Tris–glycine gels (Invitrogen/Life Technologies). Primary antibodies used were 1:1,000 pMLC-2 (Ser19) (3671S, Cell Signaling), 1:2,000 MLC-2 (M4401, Sigma-Aldrich), 1:2,000 anti-GAPDH (1D4, NB300-221, Novus Biologicals), 1:2,000 anti-β-actin (C4, sc-4778, Santa Cruz) and 1:2,000 anti-α-tubulin (T5168, Sigma-Aldrich). All secondary antibodies (anti-rabbit IgG, NA934V; anti-mouse IgG, NXA931 from GE Healthcare) were used at 1:5,000 for 1 h at room temperature.

**Quantification of western blots.** Protein levels relative to their corresponding loading control (GAPDH) were quantified using Fiji. A rectangular region of interest was drawn around the protein band, and intensity in the box was measured using the integrated density (IntDen) function in Fiji. A second region of interest of the same dimensions was then used to measure the background intensity in a region of the blot image in an area devoid of any bands. The background intensity was subtracted from the protein intensity. This procedure was carried out for all the proteins of interest and normalized to the background-subtracted intensity of the corresponding GAPDH bands.

**Quantification of cortical MYH9-GFP intensity.** To determine the cortex-to-cytoplasm ratio for MYH9, images of cells expressing MYH9-GFP were segmented on the basis of the MYH9 signal, and an average linescan of 100 pixels (with the peak of the cortical signal in the middle) was extracted, as for cortex thickness measurements. The cytoplasmic background intensity was defined as the mean intensity of the first 20 pixels of the linescan (that is, in a ~1.4 µm region, ~5.5 µm away from the peak cortical signal), and the cortex intensity was defined as the mean intensity of the 13 pixels surrounding the peak of the cortical signal (that is, within about a 900 nm region around the peak). These ranges were optimized on the basis of visual inspection of the linescans.

**RNA extraction and qPCR.** Total RNA from HeLa cells was extracted using the RNeasy Mini Kit (Qiagen). Total RNA was reverse-transcribed using a cDNA Reverse Transcription Kit (Applied Biosystems) following the manufacturer's instructions. Gene expression levels of endogenous controls GAPDH and beta-actin (ACTB) were determined using pre-validated TaqMan Gene Expression Assays (Applied Biosystems). Expression levels of queried and control genes were determined using assays designed with the Universal Probe Library from Roche. The PCR reactions were carried out on an ABI Real Time 7900HT cycler and analysed with SDS 2.2 software. qPCR was carried out with TaqMan Gene Expression Master Mix (Applied Biosystems), and all samples were tested in duplicate. mRNA levels of queried genes were normalized to the averaged levels of GAPDH and ACTB, and relative abundance was calculated by normalizing values from cells treated with control and targeted siRNA pools by dividing by the control value. The genes tested and corresponding forward and reverse primers are listed in Supplementary Table 3.

**SEM.** Sample preparation for SEM was carried out using a protocol detailed in ref. 34 with minor modifications. Briefly, cell-cycle synchronized cells (in interphase or mitosis) were plated onto 12 mm etched grid coverslips (catalogue no. 1943-10012A, SciQuip). Immediately before fixation, the cells were washed with PBS and transferred to cytoskeleton buffer (50 mM imidazole, 50 mM KCl, 0.5 mM MgCl<sub>2</sub>, 0.1 mM EDTA, 1 mM EGTA, pH 6.8) containing 0.5% Triton-X and 0.25% glutaraldehyde for 5 min. This first fixation/extraction was followed by a second extraction using 2% Triton-X and 1% CHAPS in cytoskeleton buffer for 5 min before washing the coverslips three times with cytoskeleton buffer. The rest of the protocol was identical to the protocol described in ref. 34. The cells were stained with 4,6-diamidino-2-phenylindole (1:1,000) and imaged for identification of coordinates of interphase and mitotic cells on grid coverslips. The cells were then dehydrated with serial ethanol dilutions, dried in a critical point dryer, coated with 5–6 nm platinum-palladium and imaged using the in-lens detector of a JEOL7401 field emission scanning electron microscope (JEOL).

**Quantification of holes in SEM images.** 400 pixels × 400 pixels (532 µm × 532 µm) sections were cropped from SEM images for HeLa and S-HeLa focusing on regions devoid of microvilli. Using a custom plugin developed in Fiji, pores were segmented in a semi-automated manner through intensity thresholding and size exclusion. Pore contours were then corrected manually as necessary. From the final segmentation mask, areas of holes were calculated and used to quantify the distribution of pore sizes and the percentage of area covered by pores.

**Cortex tension measurements.** For tension measurements, cells were resuspended in 10% fetal bovine serum Leibovitz's L-15 medium (Gibco, Life Technologies) before each experiment and plated on glass-bottom dishes (HBST-3522, WillCo Well).

To visualize the cell periphery, CellMask Deep Red plasma membrane stain (Life Technologies) was added to a final concentration of  $0.5 \mu\text{g ml}^{-1}$ . To verify the cell-cycle stage, DNA was labelled with Hoechst 33342 (Life Technologies) at a final concentration of  $10 \mu\text{g ml}^{-1}$ .

Tension measurements were made using a Nanowizard1 atomic force microscope (JPK Instruments) mounted on an IX81 inverted confocal microscope (Olympus). Tipless silicon nitride cantilevers (HQ-CSC38/tipless/NoAl, MikroMasch) were chosen with a nominal spring constant of  $0.03\text{--}0.09 \text{ N m}^{-1}$ . Sensitivity was calibrated by acquiring a force curve on a glass coverslip and spring constant was calibrated by the thermal noise fluctuation method. The spring constant estimated for each experiment ranged between  $0.07$  and  $0.12 \text{ N m}^{-1}$ . The calibrated cantilever was positioned within  $15 \mu\text{m}$  above the selected cell and lowered at a speed of  $0.5 \mu\text{m s}^{-1}$ . We chose a set-point force of  $10 \text{ nN}$ , which produced an average cell compression of  $1\text{--}4 \mu\text{m}$ . During the constant height compression (for  $300 \text{ s}$ ), the force acting on the cantilever was recorded. After initial force relaxation, the force value was measured (red arrow, Supplementary Fig. 1c) and a confocal stack of the cell for cell height measurement was acquired using a  $\times 60/1.35$  numerical aperture UPlanSAPO oil immersion objective (Olympus) (Supplementary Fig. 1a).

The calculation of cortex tension is based on ref. 25. Briefly, neglecting the angle of the cantilever with respect to the dish ( $\sim 8^\circ$ ) and assuming negligible adhesion between the cell and the dish and cantilever, the force balance at the contact point reads:

$$T = \frac{F \left( \frac{r_{\text{mid}}^2}{r_c^2} - 1 \right)}{2\pi r_{\text{mid}}} \quad (1)$$

where  $r_{\text{mid}}$  is the radius of the maximum cross-sectional area of the selected cell (orange line in Supplementary Fig. 1b),  $r_c$  is the radius of the contact area of the cell with the cantilever (blue line in Supplementary Fig. 1b) and  $F$  is the force exerted by the cell on the cantilever (Supplementary Fig. 1c). To avoid errors due to direct measurement of  $r_c$ , the contact radius was calculated using the following formula<sup>51</sup>:

$$A_c = A_{\text{mid}} - \left( \frac{\pi}{4} \right) h_{\text{cell}}^2 \quad (2)$$

where  $A_c$  is the contact area between the cell and the cantilever,  $A_{\text{mid}}$  is the cell maximum cross-sectional area and  $h_{\text{cell}}$  is the cell height (green line, Supplementary Fig. 1b).  $h_{\text{cell}}$  was extracted from the reconstructed confocal stack of the plasma membrane. To account for optical aberrations in cell height measurements due to mismatch in refractive index between the objective immersion medium, glass, cell cytoplasm and culture medium<sup>52</sup>, we applied a correction factor estimated following the method similar to that described in ref. 53. In brief, we used mESCs, which are small enough for their size to be directly measured using the AFM piezo motor (limited to a range of  $15 \mu\text{m}$ ), and compared cell heights obtained from confocal stacks with heights from direct AFM measurements<sup>51</sup>. Linear fitting was then used to compute the correction factor relating the apparent cell height from confocal stacks to the AFM-measured height (Supplementary Fig. 1d). This correction factor was then applied to calculate  $h_{\text{cell}}$  for larger cells for which only confocal microscopy measurements could be used. Cortical tension was then calculated using equation (1).

**3D Simulations of tension generation in the cortex.** We generated 3D simulations of a cortical network with three components: actin filaments, myosin minifilaments and crosslinkers (Fig. 4a and Supplementary Fig. 5a). Actin filaments and myosin minifilaments are modelled as rigid rods with finite lengths  $l_a$  and  $l_m$ , respectively. Myosin minifilament heads interact with actin filaments through a spring-like interaction. Similarly, crosslinkers that attach two actin filaments are treated as short springs.

The simulation is initialized as  $N_f$  actin filaments are placed within a box of square surface (side width  $W$ ) and seeding thickness  $h_0$  (Fig. 4b and Supplementary Fig. 5b). Crosslinkers are introduced into the system with an actin-binding

probability  $p_x$ . Finally, myosin minifilaments initially bind to actin filaments in a straight, unstretched configuration.

After initialization, the simulation is updated in two stages at every step of iteration. In the first stage, myosin minifilaments bind and unbind, and bound minifilaments walk towards plus ends of actin filaments. In the second stage, the network configuration is mechanically relaxed.

The simulation is run for  $200 \text{ s}$  and updated every  $10^{-3} \text{ s}$ . Network surface tension is measured by slicing the network with a plane and calculating the total force  $F$  acting in the direction normal to that plane (Fig. 4avi). Tension is then calculated by dividing  $F$  by the width of the simulation box  $W$ . To obtain average steady-state tensions plotted in Figs 4d and 5a, tension values are averaged between  $t_0 = 25 \text{ s}$  and the total simulation time of  $200 \text{ s}$ .

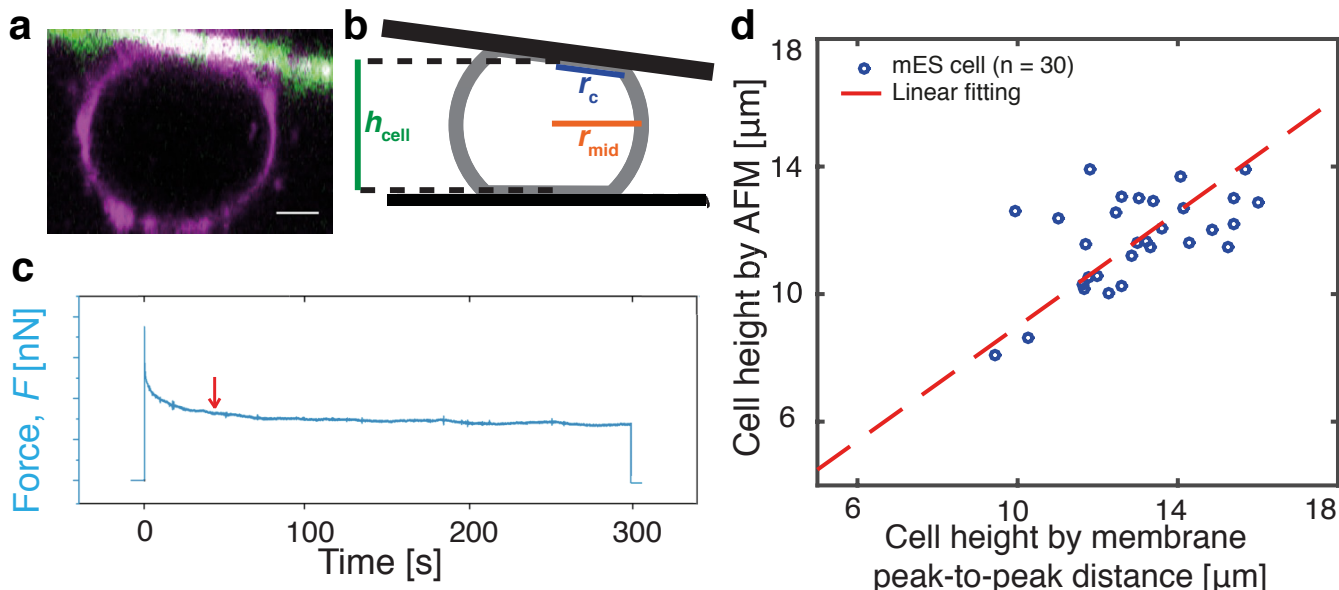
To explore the relationship between actin filament length and tension in the network, varying actin filament lengths were used as input while keeping the mean actin density constant in the network, in accordance with experimental observations. A more complete description of the model can be found in the Supplementary Note.

**Statistics and reproducibility.** Boxes in all box plots extend from the 25th to 75th percentiles, with a line at the median. Whiskers extend to  $\times 1.5$  the interquartile range or to the max/min data points if they fall within 1.5 times the interquartile range. Each dot on the box plots represents a measurement from a single cell. For comparisons of means between categories, Welch's *t*-test (two tailed, no assumption of variance) was carried out, and *P*-values were obtained from a *t*-value lookup table. Welch's *t*-test *P*-values: \**P* < 0.05, \*\**P* < 0.01, and \*\*\**P* < 0.001. For the cortex tension data in Fig. 1d (left), outliers were determined on the basis of the following criteria: (1) deviation from the majority of the data on the basis of visual inspection of the normal probability plot, (2) values greater than 1.5 times the interquartile range beyond the third quartile<sup>54</sup>, (3) modified *Z*-score greater than 3.5 (see ref. 55), (4) Grubbs' test statistic greater than the critical value (at *P* < 0.05)<sup>56</sup>. For the Grubbs' test, tests for each outlier were carried out sequentially, removing outliers individually. All statistical analyses and plotting were carried out using Python ([www.python.org](http://www.python.org)), using the Numeric Python (NumPy), Scientific Python (SciPy) and Matplotlib packages.

**Code availability.** Code used to perform and analyse simulations is publicly available at <https://github.com/PaluchLabUCL/CortexDynamicsNCB>. Code used to segment cells and analyse linescans for thickness/density extraction is publicly available at <https://github.com/PaluchLabUCL/CortexThicknessAnalysis>.

**Data availability.** All data supporting the conclusions here are available from the authors on reasonable request.

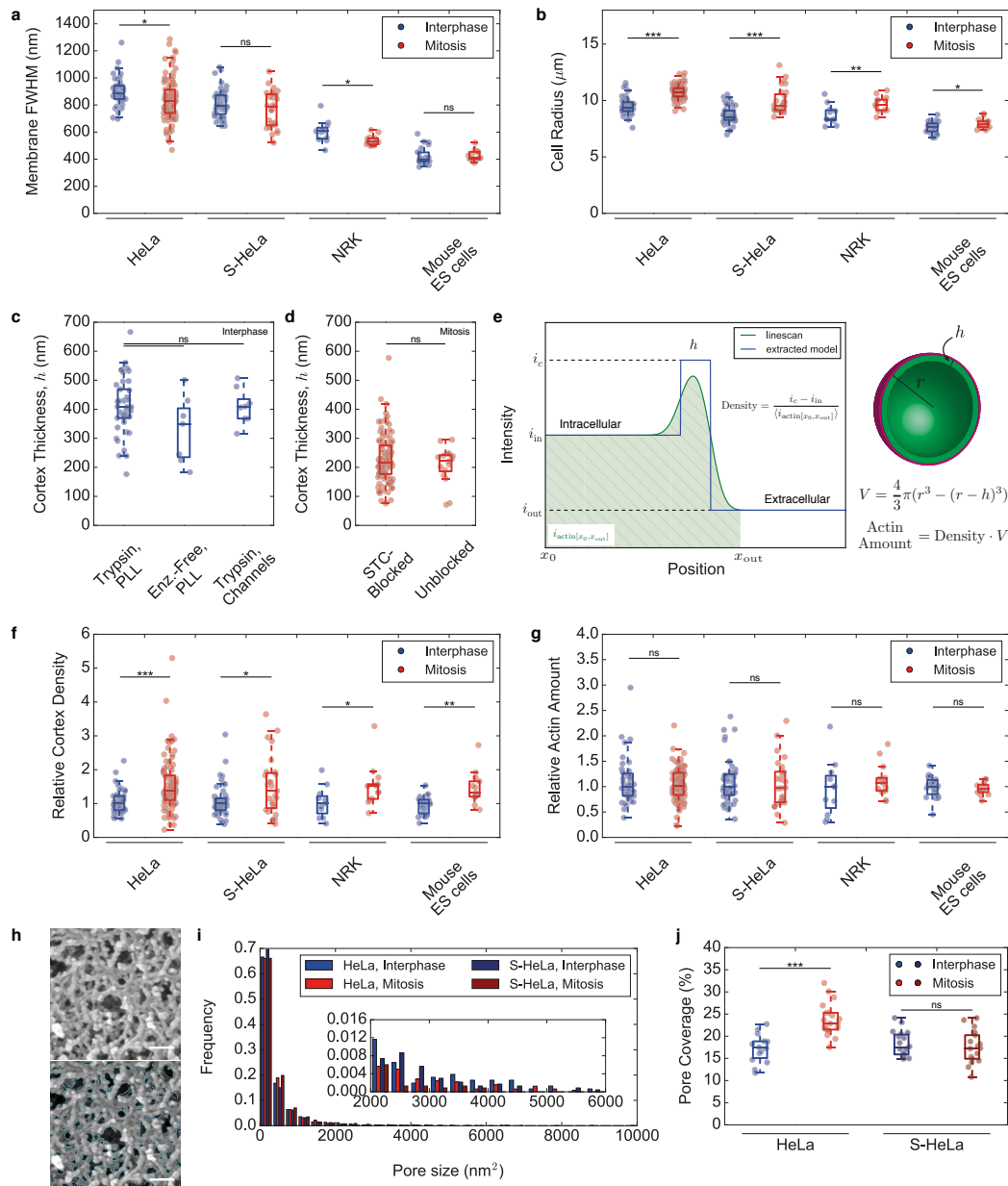
48. Pagliara, S. *et al.* Auxetic nuclei in embryonic stem cells exiting pluripotency. *Nat. Mater.* **13**, 638–644 (2014).
49. Skoufias, D. A. *et al.* S-trityl-L-cysteine is a reversible, tight binding inhibitor of the human kinesin Eg5 that specifically blocks mitotic progression. *J. Biol. Chem.* **281**, 17559–17569 (2006).
50. Schindelin, J. *et al.* Fiji: an open-source platform for biological-image analysis. *Nat. Methods* **9**, 676–682 (2012).
51. Stewart, M. P., Toyoda, Y., Hyman, A. A. & Muller, D. J. Tracking mechanics and volume of globular cells with atomic force microscopy using a constant-height clamp. *Nat. Protoc.* **7**, 143–154 (2012).
52. Hell, S., Reiner, G., Cremer, C. & Stelzer, E. H. K. Aberrations in confocal fluorescence microscopy induced by mismatches in refractive index. *J. Microsc.* **169**, 391–405 (1993).
53. Diaspro, A., Federici, F. & Robello, M. Influence of refractive-index mismatch in high-resolution three-dimensional confocal microscopy. *Appl. Opt.* **41**, 685–690 (2002).
54. Tukey, J. W. *Exploratory Data Analysis* (Addison-Wesley, 1977).
55. Igglewick, B. & Hoaglin, D. C. *How to Detect and Handle Outliers* (ASQC Quality Press, 1993).
56. NIST/SEMATECH e-Handbook of Statistical Methods (eds Croarkin, C. & Tobias, P.) (2010); <http://www.itl.nist.gov/div898/handbook>



**Supplementary Figure 1** Cortex tension measurements using tipless cantilever atomic force microscopy (AFM). (a) Representative YZ image of a mitotic adherent HeLa cell with plasma membrane labelled using CellMask Deep Red™ (magenta) and cantilever visualized by laser reflection (green). Scale bar = 5  $\mu\text{m}$ . (b) Schematic of tipless cantilever AFM assay.  $r_{mid}$ : radius of the maximum cross sectional area of the cell;  $r_c$ : radius of the contact area of the cell with the cantilever; and  $h_{cell}$ : height of the cell. (c) AFM force curve from a cell compression experiment. Red arrow indicates the time point after initial force relaxation, at which cell height is recorded. Confocal

stack acquisition for cell height recording induces force fluctuations (not displayed), therefore force is measured before the confocal stack is acquired. (d) Calculation of the correction coefficient for refractive index mismatches. Plot of mES cell height values directly measured by AFM vs. those extracted from confocal stacks of mESCs with the membrane labelled (peak-to-peak distance). The slope calculated from linear fitting was used to correct for optical aberrations due to refractive index mismatch in cell height measurements, see Methods for details. Points represent individual measurements ( $n=30$  cells from 3 independent experiments).

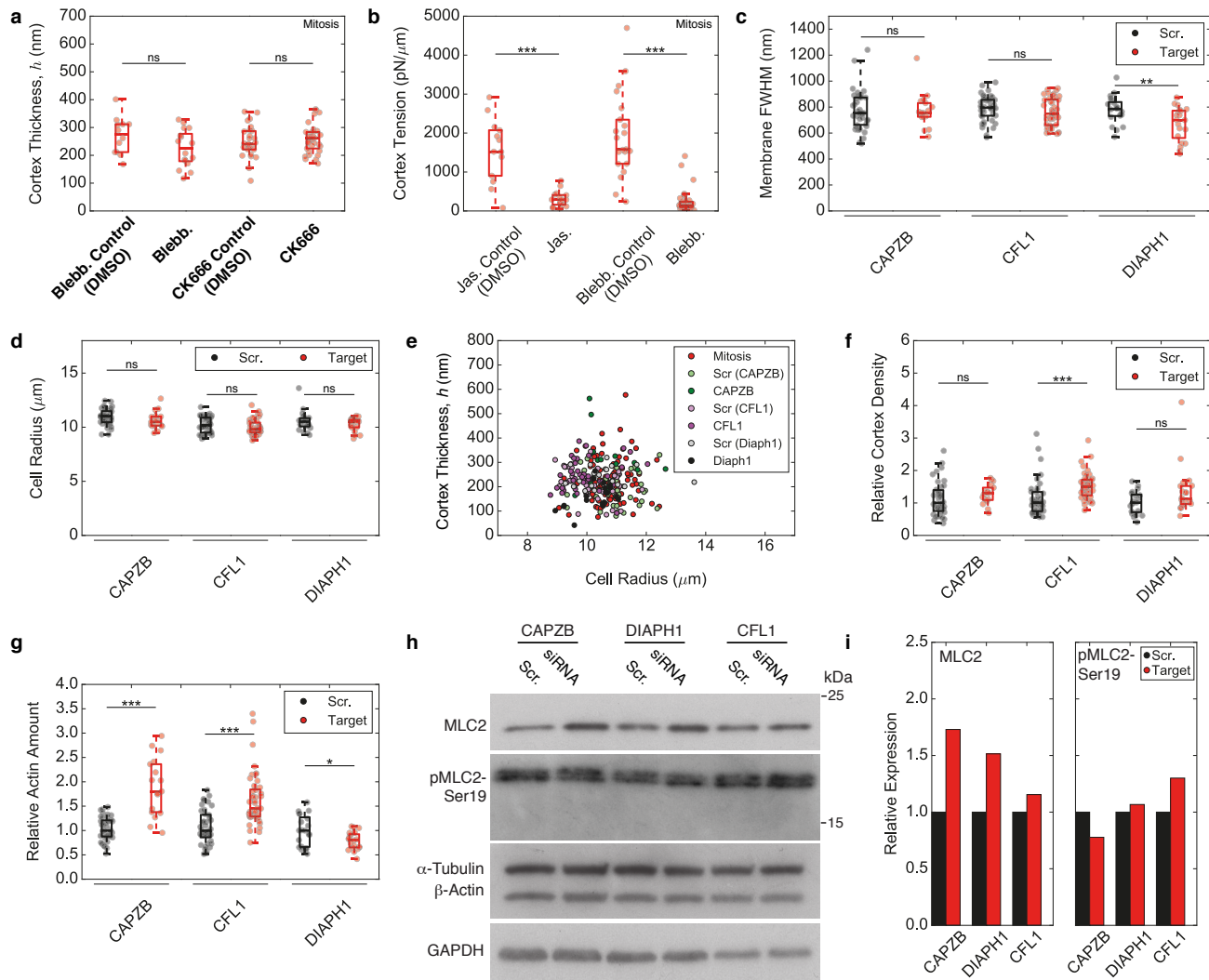
## SUPPLEMENTARY INFORMATION



**Supplementary Figure 2** Extended measurements of cortex properties in interphase and mitosis. (a,b) Full width at half-maximum (FWHM) of membrane linescans ( $p=0.050, 0.16, 0.025, 0.82$ ) (a) and cell radii ( $p=9.8 \times 10^{-13}, 7.2 \times 10^{-6}, 0.0062, 0.048$ ) (b) for different cell lines in interphase and mitosis ( $n=41, 100, 47, 27, 11, 13, 22, 13$  individual measurements from 2-13 independent experiments). (c) Cortex thickness measurements for interphase HeLa cells detached using trypsin or enzyme-free detachment (Enz.-Free) and immobilized by centrifugation on Poly-L-Lysine (PLL)-coated dishes or by confining the cells in 25  $\mu\text{m}$  microchannels (Channels;  $n=41, 7, 8$  individual measurements from 1-3 independent experiments;  $p=0.11, 0.98$ ). (d) Cortex thickness measurements for HeLa cells blocked in prometaphase with S-Trityl-L-cysteine (STC-Blocked) and unblocked mitotic HeLa cells identified based on morphology and chromosome appearance ( $n=100, 16$  individual measurements from 13 (STC-blocked) and 1 (unblocked) independent experiments;  $p=0.2565$ ). (e) Left: calculation of average cortical actin density using the cortical thickness extraction method (Ref. 24 in the main text). Right: calculation of total cortical actin amount using the measured cell radius ( $r$ ) and cortex thickness ( $h$ ). (f,g) Relative cortex

density ( $p=1.2 \times 10^{-6}, 0.018, 0.032, 0.0023$ ) (f) and amount ( $p=0.47, 0.66, 0.40, 0.53$ ) (g) for different cell lines in interphase and mitosis. Values were normalized by dividing by the median of the interphase value for each cell line ( $n=41, 100, 47, 27, 11, 13, 22, 13$  individual cell measurements from 2-13 independent experiments). (h) Example segmentation mask (bottom) applied to a scanning electron micrograph of membrane-extracted cortices (top, from Fig. 1g). Images are representative of 17 regions from 8 cells (2 independent experiments). Scale bars = 100 nm. (i) Frequency distribution of pore sizes for adherent HeLa and S-HeLa cells in interphase and mitosis ( $n=14, 19, 18, 17$  regions from 9, 13, 8, 8 cells from 2 independent experiments). Size distributions were comparable between interphase and mitosis, with slightly more large pores in interphase compared to metaphase (inset). (j) Pore coverage (%) in HeLa and S-HeLa cells in interphase and mitosis from regions analysed in (i) ( $p=4.3 \times 10^{-6}, 0.59$ ). The average pore coverage was unchanged in S-HeLa cells and slightly higher in mitosis in HeLa cells. However, SEM only probes the outer surface of the cortex; it is thus difficult to draw conclusions about overall cortical actin density from this analysis. For all panels, Welch's t-test p-values: ns  $p>0.05$ , \*  $p<0.05$ , \*\*  $p<0.01$ , \*\*\*  $p<0.001$ .

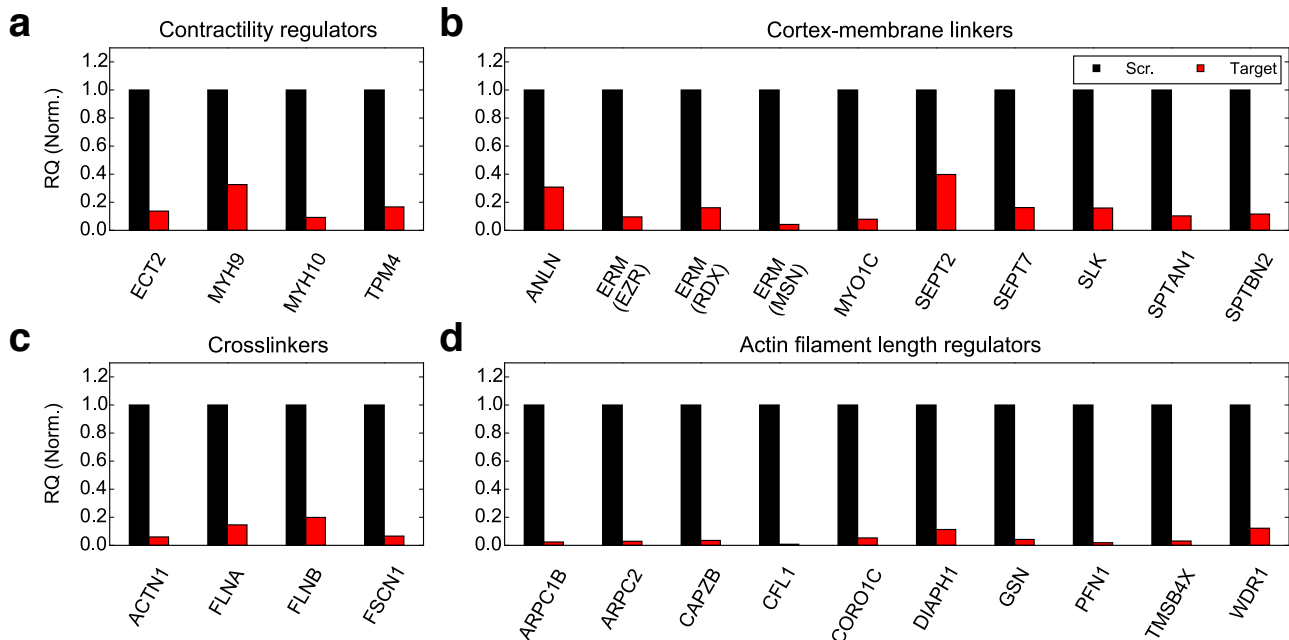
## SUPPLEMENTARY INFORMATION



**Supplementary Figure 3** Extended measurements of cortex properties upon depletion of cortex thickness regulators. (a) Cortex thickness measurements for mitotic HeLa cells treated with the myosin-II inhibitor Blebbistatin (Blebb.), the Arp2/3 inhibitor CK-666 and corresponding DMSO controls ( $n=12, 16, 27, 33$  individual measurements from 2-3 independent experiments;  $p=0.078, 0.47$ ). (b) Cortex tension measurements following treatment with the actin stabilizing drug Jasplakinolide (Jas.), Blebbistatin (Blebb.) and corresponding DMSO controls ( $n=13, 16, 21, 38$  individual measurements from 3 independent experiments;  $p=8.1\times 10^{-5}, 3.4\times 10^{-7}$ ). (c,d) Boxplot comparing the full width at half maximum (FWHM) of the membrane linescan ( $p=0.94, 0.20, 0.0065$ ) (c) and cell radii ( $p=0.19, 0.084, 0.31$ ) (d) in mitotic HeLa cells following siRNA against *CAPZB*, *CFL1* and *DIAPH1* ( $n=38, 17, 40, 44, 20, 20$  individual measurements from 3-4 independent experiments). The membrane FWHM was  $\sim 10\text{-}15\%$  smaller in *DIAPH1* knockdown cells, not enough to account for the  $\sim 60\%$  reduction in cortex thickness. (e) Scatter plot of cortex thickness vs. cell radius for all measured conditions in mitotic HeLa cells (untreated, target knockdowns

and corresponding scrambled controls [Scr.]). (f,g) Relative cortex density ( $p=0.23, 0.0008, 0.059$ ) (f) and amount ( $p=1.4\times 10^{-5}, 3.6\times 10^{-7}, 0.016$ ) (g) in mitotic HeLa cells treated with siRNA against *CAPZB*, *CFL1* and *DIAPH1* (Target) and corresponding scrambled controls (Scr.). Values were normalized by dividing by the median of the corresponding Scr. control ( $n=38, 17, 40, 44, 20, 20$  individual measurements from 3-4 independent experiments). Cortex density and amount were calculated as described in Supplementary Fig. 2e. (h) Western blot showing the levels of active myosin light chain (pMLC2-Ser19) and total myosin light chain (MLC2) in whole cell lysates of mitotic HeLa cells treated with siRNA against *CAPZB*, *DIAPH1*, or *CFL1*, and corresponding scrambled (Scr.) controls. GAPDH,  $\beta$ -Actin and  $\alpha$ -Tubulin were used as loading controls. Blots are representative of at least 3 independent experiments. Uncropped Western blots are provided in Supplementary Fig. 7. (i) Quantification of the Western blot shown in panel h, showing the mitotic levels of MLC2 and pMLC2-Ser19 in each knockdown relative to its Scr. siRNA control. For all panels, Welch's t-test p-values: ns $p>0.05$ , \* $p<0.05$ , \*\* $p<0.01$ , \*\*\* $p<0.001$ .

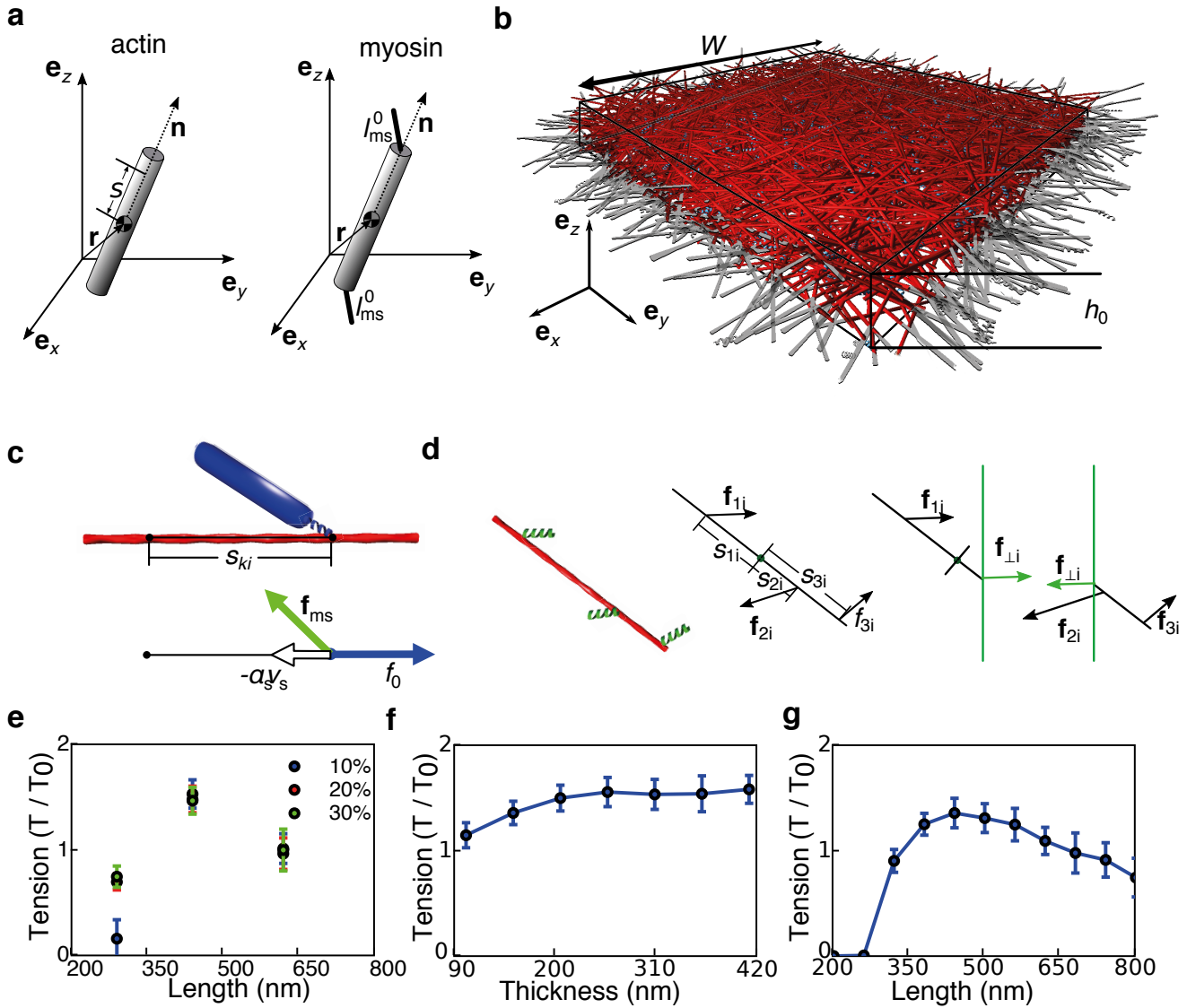
## SUPPLEMENTARY INFORMATION



**Supplementary Figure 4** Depletion efficiency for the targeted siRNA screen for cortex thickness regulators. The bar plot shows the mRNA expression levels (RQ) in adherent HeLa cells treated with siRNA against various ABPs normalized to mRNA levels in control non-silencing pools (RQ (Norm.)). RQ levels were calculated by normalizing mRNA levels of queried genes to

the averaged levels of GAPDH and ACTB. Relative mRNA abundance (RQ (Norm.)) was then calculated by dividing by the RQ value for control pools. Differences were considered significant if RQ (Norm.) was reduced by at least 40%. qPCR analysis was performed once for all siRNA conditions. For hits from the targeted ABP screen, Western blots were performed (Fig. 3b).

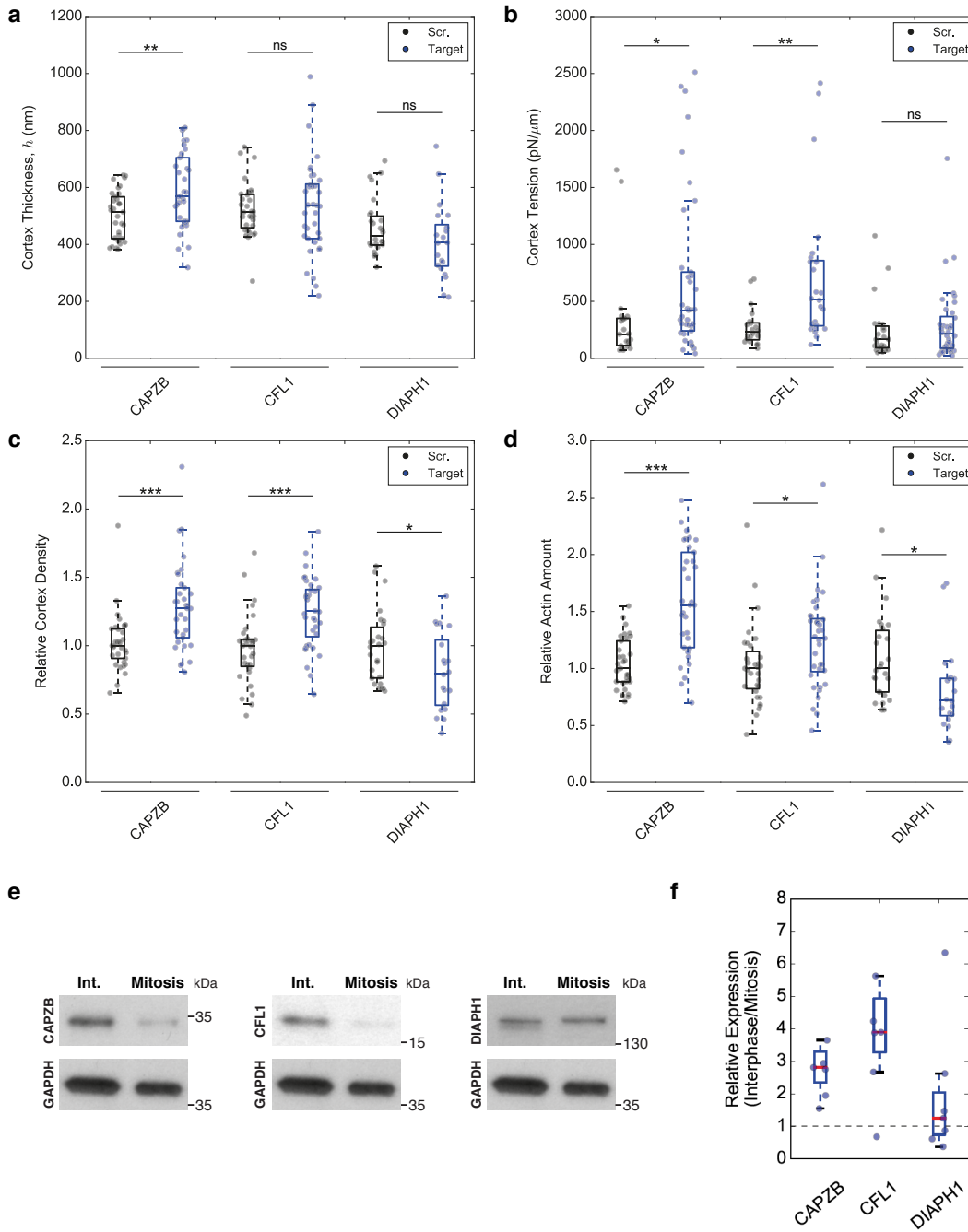
## SUPPLEMENTARY INFORMATION



**Supplementary Figure 5** Computer simulations of tension generation in a crosslinked actomyosin cortex. (a) Actin filament representation (left):  $r$  is the centre of mass,  $s$  describes a position along the filament and the unit vector  $n$  is oriented towards the plus end of the filament. Myosin minifilament representation (right) with the centre of mass ( $r$ ), orientation vector ( $n$ ) and the two connecting heads. (b) Initialized network with a seeding thickness  $h_0$  and width  $W$ . Grayed filaments cross periodic boundaries in the  $x$  and  $y$  directions. (c) Myosin head attachment (top) and force balance on the myosin-actin attachment point (bottom).  $v_s$  is the velocity of the myosin,  $a_s$  is a friction coefficient,  $f_0$  is the myosin stall force and  $f_{ms}$  is the spring force of the myosin head. (d) Schematic of actin filament  $i$  with three springs connected, force balance on the filament, and sliced filament for surface

tension measurement. The resulting force  $f^\wedge$ , along the normal of the slicing plane is used for calculating the total force. (e) Tension as a function of mean filament length for simulations where filament lengths were chosen according to a Gaussian distribution around a mean length. The standard deviations of the Gaussian distribution were 10% (blue), 20% (red), and 30% (green) of the mean length. (f) Tension as a function of the seeding thickness at constant filament length, density and number of motors. Seeding thickness is varied by changing the number of filaments. (g) Tension as a function of filament length at constant seeding thickness and density. The total number of filaments is adjusted to keep the total amount (length) of actin,  $L_a = N_f l_{a0}$  constant. For (e-g), each point represents the mean of 9 simulations,  $\pm SD$ . Tensions are normalized to  $T_0 = 230 \text{ pN}/\mu\text{m}$ .

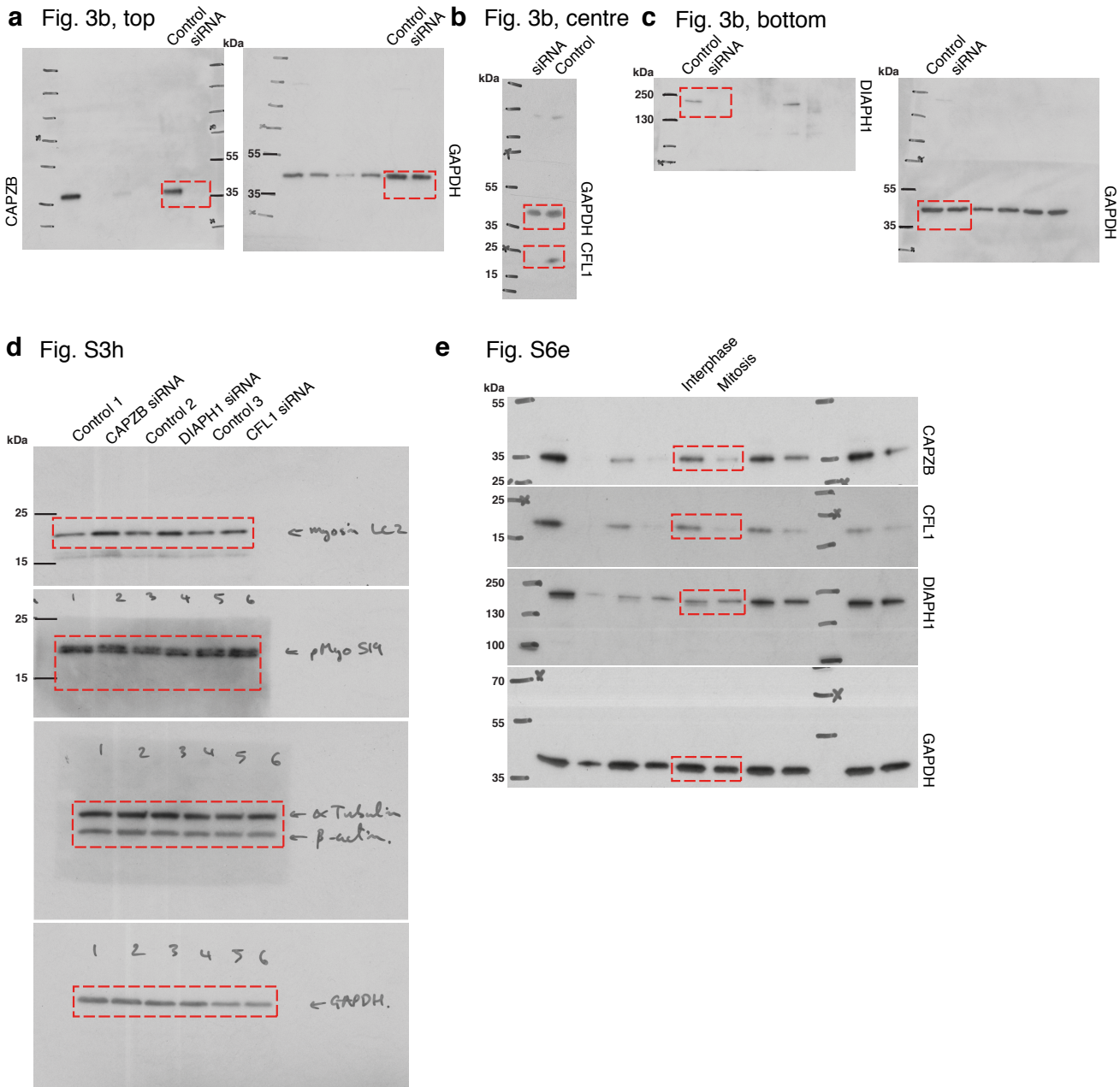
## SUPPLEMENTARY INFORMATION



**Supplementary Figure 6** Effect of mitotic thickness regulators on the interphase cortex. Boxplots comparing (a) cortex thickness ( $p=0.0016$ , 0.79, 0.16), (b) cortex tension ( $p=0.018$ , 0.0025, 0.48), (c) relative cortex density ( $p=0.0002$ ,  $6.3 \times 10^{-5}$ , 0.031), and (d) relative actin amount ( $p=1.5 \times 10^{-7}$ , 0.023, 0.014) between interphase HeLa cells treated with siRNA targeted against *CAPZB*, *CFL1* or *DIAPH1* (Target, blue) or the corresponding scrambled siRNAs (Scr., black). Relative values were normalized to the median of the corresponding Scr. control. Points represent individual measurements ( $n=33$ , 33, 31, 36, 26, 20 cells from 3 independent experiments for thickness, density and amount measurements;  $n=22$ , 37, 20, 24, 23, 36 cells from 3-4 independent experiments for cortex tension measurements). Cortex thickness increased upon depletion of *CAPZB*, but did not significantly change upon *CFL1* and *DIAPH1* knockdown. Cortex tension increased upon depletion of *CAPZB* and *CFL1* (as previously reported for *CFL1*, Ref [13]), but did not significantly change upon *DIAPH1* depletion. These results could suggest a mitosis-specific

role of *DIAPH1* in thickness/tension regulation. (e) Western blots showing the levels of *CAPZB*, *CFL1*, and *DIAPH1* in whole cell lysates of interphase (Thymidine-blocked) and mitotic (STLC-blocked) HeLa cells. GAPDH was used as a loading control. Blots are representative from 7 independent experiments. (f) Boxplots comparing the interphase/mitosis ratio of normalized *CAPZB*, *CFL1*, and *DIAPH1* expression from 7 independent experiments. The whole cell levels of both *CAPZB* and *CFL1* were higher in interphase than in mitosis, while *DIAPH1* levels did not change. This suggests that the hits identified in our screen do not directly control the cortical thinning between interphase and mitosis. However, it is important to note that Western blot analysis reflects whole cell levels and may not reflect changes in cortical localization. Furthermore, these experiments do not take into account any possible post-translational modification of these proteins. Dotted line (ratio = 1) signifies no change in levels between interphase and mitosis. Uncropped western blots are provided in Supplementary Fig. 7.

## SUPPLEMENTARY INFORMATION



**Supplementary Figure 7** Uncropped Western blots for Fig. 3b, Supplementary Fig. 3h and Supplementary Figure 6e. Red dotted lines indicate regions that were cropped for the figures.

## SUPPLEMENTARY INFORMATION

### Supplementary Tables Legends

**Supplementary Table 1** Thickness and volume changes between interphase and mitosis. Expected changes in mitotic cortical thickness ( $h_{expected,m}$ ) assuming conserved cortex volume was calculated from the median radius in interphase ( $r_i$ ), median radius in mitosis ( $r_m$ ) and median cortex thickness in interphase ( $h_i$ ) using the formula,  $h_{expected,m} \approx (r_i^2 * h_i)/r_m^2$ , and compared to the measured mitotic cortex thickness ( $h_m$ ).

**Supplementary Table 2** Detailed information about siRNA knockdown conditions in Fig. 2. The table includes supplementary references 16-18 (see Supplementary Note). Each ABP was depleted using siRNA previously shown to reduce expression, or siRNA pools.

**Supplementary Table 3** Primers used for qPCR to test siRNA knockdown efficiency in Supplementary Fig. 4.

**Supplementary Table 4** Median cortex stress. Median cortical stress was calculated from the ratio of median tension and median thickness for all conditions.

**Supplementary Table 5** Simulation Parameters. Whenever possible, simulation parameters were estimated from literature or chosen so that the appearance of the simulated cortex is comparable to experimental observations. The table includes supplementary references 1 and 5 (see Supplementary Note).

### Supplementary Video Legends

**Supplementary Video 1** Simulation of a 3D cortex with 200 nm long actin filaments. *Left:* xy and xz views of the simulated cortex with  $l_a = 200$  nm. *Right:* Evolution of tension over time during the simulation run.

**Supplementary Video 2** Simulation of a 3D cortex with 500 nm long actin filaments. *Left:* xy and xz views of the simulated cortex with  $l_a = 500$  nm. *Right:* Evolution of tension over time during the simulation run.

**Supplementary Video 3** Simulation of a 3D cortex with 740 nm long actin filaments. *Left:* xy and xz views of the simulated cortex with  $l_a = 740$  nm. *Right:* Evolution of tension over time during the simulation run.

**SUPPLEMENTARY NOTE FOR:**

**Actin cortex architecture regulates cell surface tension**

Priyamvada Chugh, Andrew G. Clark, Matthew B. Smith, Davide A. D. Cassani, Kai Dierkes,  
Anan Ragab, Philippe P. Roux, Guillaume Charras, Guillaume Salbreux and Ewa K. Paluch

# **Contents**

<b>Description of cortex simulations.</b>	<b>2</b>
<b>Supplementary References.</b>	<b>8</b>

## Description of cortex simulations.

We introduce three components in our simulations: actin filaments, crosslinkers, and myosin minifilaments (Fig. 4a). A list of the simulations parameters is given in Supplementary Table 5.

Actin filaments are treated as rigid rods (see Discussion of model assumptions below) with a finite length,  $l_a$ , ranging between 200 nm and 800 nm for the different simulation conditions. For each simulation, all filaments had the same length (we checked the robustness of our conclusions by introducing a Gaussian distribution in filament length, Supplementary Fig. 5e). The unit vector giving the orientation of filament  $i$  is denoted  $\mathbf{n}_i$  (Supplementary Fig. 5a), and points towards the plus end of the actin filament.

Myosin minifilaments are simulated as three distinct sections, a "bare zone" and two connecting heads, with a total length of approximately 300 nm (1). The bare zone is simulated as a rigid stalk with a length  $l_m = 200$  nm. At both ends of the bare zone, the connecting heads can bind to actin filaments (Supplementary Fig. 5a). The connecting heads are treated as springs with stiffness  $k_{ms}$  and reference length of  $l_{ms}^0 = 50$  nm, such that the force in the end-spring,  $f_{ms}$ , is:

$$f_{ms} = k_{ms} (l_{ms} - l_{ms}^0), \quad (1)$$

where  $l_{ms}$  is the distance between the end of the bare zone and the point on the actin filament that the connecting head is attached to. The junctions between the minifilament bare zone and either end-spring, as well as junction between the end-springs and actin filament, can freely rotate. The position of attachment for myosin minifilament  $k$  on actin filament  $i$  is measured as the distance from the center of mass of the actin filament, and is denoted  $s_{ki}$  (Supplementary Fig. 5c).

Crosslinkers are treated as short springs that attach to two actin filaments (Fig. 4a). Crosslinkers have a stiffness  $k_x$  and a resting length  $l_x^0 = 50$  nm, such that the force produced by a crosslinker is defined as:

$$f_x = k_x (l_x - l_x^0), \quad (2)$$

where  $l_x$  is the distance between the points of attachment on the actin filaments the crosslinker is attached to.

We simulate the network in three dimensions,  $x, y, z$ . We denote the cartesian unit vectors  $\mathbf{e}_x, \mathbf{e}_y, \mathbf{e}_z$  (Supplementary Fig. 5a, b). The boundary conditions in the  $x$  and  $y$  directions are periodic, with the width,  $W$ , equal to 2.5  $\mu\text{m}$  (Supplementary Fig. 5b). There are no boundary conditions in the  $z$  direction.

## Initialization

The simulation is initialized by placing  $N_f$  actin filaments within the simulation box, at random positions along the  $x$  and  $y$  directions. In the  $z$  direction filament positions are limited by the seeding thickness,  $h_0$  (Supplementary Fig. 5b). Their initial  $z$  position is placed randomly within the interval  $-h_0/2 \leq z \leq h_0/2$  in the  $z$  direction. Filament orientations can be written

in spherical coordinate:

$$\mathbf{n}_i = (\sin \theta \cos \phi) \mathbf{e}_x + (\sin \theta \sin \phi) \mathbf{e}_y + (\cos \theta) \mathbf{e}_z, \quad (3)$$

where the angles  $\theta$  and  $\phi$  are taken from the probability distribution

$$P(\theta, \phi) = \frac{\sin \theta}{4\pi \sin \frac{\sigma_a}{2}} \Theta \left( \frac{\theta - \frac{\pi}{2}}{\sigma_a} \right). \quad (4)$$

The function  $\Theta(x)$  is 1 for  $-\frac{1}{2} < x < \frac{1}{2}$  and is 0 otherwise.  $P(\theta)$  is chosen such that filament orientations are uniformly distributed within the limiting angle,  $\sigma_a$ , such that  $\frac{\pi}{2} - \frac{\sigma_a}{2} < \theta < \frac{\pi}{2} + \frac{\sigma_a}{2}$ . For  $\sigma_a = 0$ , filaments are parallel to the  $x, y$  plane, and for  $\sigma_a = \pi$ , they are isotropically oriented.

The seeding thickness,  $h_0$ , is chosen to keep the mean actin length density, defined as

$$\rho_f = \frac{N_f l_a}{W^2 h_0}, \quad (5)$$

constant for the varying actin lengths. We chose a density that correspond roughly to the density observed using SEM data (Fig. 1g and Supplementary Fig. 2h, i), where about 75% of the surface was covered with actin filaments.

Crosslinkers are introduced in the simulation by looking for possible binding sites where two filaments are separated by a distance less than  $l_x^0$ . A crosslinker is then added to each potential binding site with probability  $p_x$ . Crosslinkers are added in their resting configuration by attaching one end of the crosslinker to a potential binding site on the first filament and looking for a position at distance  $l_x^0$  on the other filament. If there are two possible sites, one site is chosen randomly.

Finally, myosin minifilaments are placed by positioning one of the end-springs on a randomly chosen actin filament, and searching the remaining actin filaments within a distance  $l_m$  for potential binding sites at a distance  $l_m + 2l_{ms}^0$ . If such a binding site exists, the myosin links the two filaments in a straight, unstretched configuration. If more than one binding site exists, one site is chosen at random, and when no filaments satisfy the condition, the second end is left free and placed randomly.

## Dynamics

After initialization, the simulation runs in two phases. In the first phase, myosin minifilaments bind and unbind actin filaments, or minifilaments that are bound to an actin filament can walk towards the plus end of actin filaments. In the second phase, after every step of myosin interaction, the network is relaxed quasi-statically until a criterion defined below is met.

### Myosin binding and walking dynamics

Myosins can unbind actin filaments because they reach the end of the filament or because they spontaneously unbind. Spontaneous unbinding occurs randomly with a mean lifetime of  $\tau_m$ .

When a minifilament head binds to an actin filament, a lifetime is chosen from an exponential distribution with mean  $\tau_m$ . If the amount of time the minifilament has remained bound exceeds the chosen lifetime, the head unbinds. When both heads of a myosin minifilament are free, the myosin minifilament immediately rebinds a filament in the network at a random location, following the same procedure used during initialization. As a result, the number of myosins bound in the network is fixed.

At every step, the binding position of myosin minifilament  $k$  on filament  $i$ , denoted  $s_{ki}$ , is updated according to the following equation:

$$\alpha_s \frac{ds_{ki}}{dt} = f_0 + \mathbf{f}_{ms} \cdot \mathbf{n}_i, \quad (6)$$

where  $\alpha_s$  is an effective friction coefficient between the motor and the filament, the stall force,  $f_0$ , is an active force that is generated by the minifilament towards the plus end of the actin filament, and  $\mathbf{f}_{ms}$  is oriented from the point of attachment towards the end of the minifilament and has a magnitude set by Eq. 1. When the projection along the direction of the filament of the tension in the end-spring is equal to  $-f_0$ , the head does not move (Supplementary Fig. 5c).

## Network relaxation

After myosin binding has been updated, the network is relaxed quasi-statically, without updating myosin positions on actin filaments. Below, we denote  $t^*$  as a fictitious time coordinate used for this relaxation. Network relaxation is performed for both actin filaments and myosin minifilaments. The centers of mass,  $\mathbf{r}_i$ , and orientations,  $\mathbf{n}_i$ , are updated according to the following equations:

$$\alpha_t \frac{d\mathbf{r}_i}{dt^*} = \sum_k \mathbf{f}_{ik} \quad (7)$$

$$\alpha_r \frac{d\mathbf{n}_i}{dt^*} = -\mathbf{n}_i \times \left( \sum_k s_k \mathbf{n}_i \times \mathbf{f}_{ik} \right), \quad (8)$$

where  $\mathbf{f}_{ik}$  is the force acting on filament  $i$  by a spring-like attachment  $k$  (crosslinker or myosin head binding).  $\alpha_t$  and  $\alpha_r$  are translational and rotational fictitious friction coefficients. Steric interactions are not considered, which means filaments and crosslinkers only interact if they are bound. As a result filaments, crosslinkers, and myosins can freely pass through each other.

Iteration is performed by discretising equations 7 and 8 with an Euler explicit scheme with adaptive steps. The network relaxation is performed for 10000 trial steps, or if the following criterion is satisfied. The norms of the total force and torque for each filament

$$\mathbf{f}_i = \sum_k \mathbf{f}_{ik} \quad (9)$$

$$\tau_i = \sum_k s_k \mathbf{n}_i \times \mathbf{f}_{ik} \quad (10)$$

are averaged over all actin filaments and myosin minifilaments  $i$  to obtain:

$$e = \frac{1}{N} \left[ \sum_i \frac{|\mathbf{f}_i|}{f_0} + \sum_i \frac{|\tau_i|}{f_0 l_0} \right] \quad (11)$$

where  $N$  is the total number of actin and myosin filaments, and  $l_0$  is a reference length set to 250 nm. The relaxation is stopped when  $e$  is less than the relaxation limit parameter  $e_{max}$  (Supplementary Table 5) and  $\max(|\mathbf{f}_i|/f_0) < 0.01$ .

## Network surface tension measurement

The network surface tension  $T$  is measured by slicing the network with a plane and calculating the total force  $F$  acting normal to the plane (Fig. 4a). The total force  $F$  is obtained by summing the forces acting within actin filaments, myosin minifilaments and crosslinkers cut by the plane (Supplementary Fig. 5d). The surface tension is then calculated according to:

$$T = \frac{F}{W} \quad (12)$$

In practice the tension is measured by slicing with two different planes, the plane perpendicular to the  $x$ -axis to measure  $T_x$ , and the plane perpendicular to the  $y$ -axis to measure  $T_y$ , both going across the center of the simulation box. The network is further relaxed to equilibrium prior to tension measurement. We then report the average surface tension  $(T_x + T_y)/2$ .

In Figures 4c, d, 5a and Supplementary Figure 5e-g, we also normalize the surface tension to a reference surface tension  $T_0$  defined as:

$$T_0 = \frac{f_0(l_m + 2l_{ms}^0) N_m}{W^2}, \quad (13)$$

which is the product of the characteristic myosin force dipole,  $f_0(l_m + 2l_{ms}^0)$ , and the two-dimensional concentration of myosins,  $N_m/W^2$ . For our choice of parameters,  $T_0 \simeq 230$  pN/ $\mu$ m.

To obtain the average tensions plotted in Figs. 4d, 5a and Supplementary Fig. 5e-g, we average the tension between  $t_0 = 25$  s and the total simulation time  $t = 200$  s.

## Local strain and network stress measurement

We now describe the calculation of strain from simulations of deformed actin networks (Fig. 5). We used projected views of the 3D network on a 2D plane. A square lattice is defined with side length  $l_l/W = 0.02$ . For each point in the lattice, a neighbourhood region is defined as the circle with radius  $l_l/4$  centered around the lattice point. For each lattice point, only filaments located within the neighbourhood are taken into account. The set of positions of points on these filaments that are closest to the lattice point is then obtained in the initial state,  $\{\mathbf{P}_i\}$  and deformed state,  $\{\mathbf{P}_f\}$ . The initial position of lattice point is repositioned to the average of the points within the neighbourhood,  $\langle\{\mathbf{P}_i\}\rangle$ . The deformation vector of each lattice point is obtained from  $\langle\{\mathbf{P}_f\}\rangle - \langle\{\mathbf{P}_i\}\rangle$ .

A set of triangles is then obtained by connecting two opposite points within each cell of the lattice. The relative change of area of each triangle under the deformation field is calculated to obtain a field of isotropic strain (Fig. 5b).

To calculate the local 2D network stress, a square lattice is defined with the same side length  $l_l/W = 0.02$ . The isotropic 2D stress acting in the center of each lattice cell,  $(T_{xx} + T_{yy})/2$ , is then calculated.

## Additional simulations

### Variability in filament length

In the actin cortex, filaments may have varying lengths. To test how actin filaments length distribution affects our results, we ran simulations where the filament lengths have a Gaussian distribution with standard deviations of 10%, 20%, and 30% of the mean length. These simulations were run for three different average filament lengths,  $l_a = 290$  nm,  $l_a = 440$  nm, and  $l_a = 620$  nm, which correspond to three regions of tension generation: low tension, peak tension and medium tension respectively (Supplementary Fig. 5e). We find that the network tension increases for short filament networks when the standard deviation of filament length increases, but a peak tension still appears at intermediate filament lengths for all standard deviations tested.

### Changing cortex seeding thickness at fixed filament length

We then tested whether the choice of seeding thickness of the simulated cortex alone affects the magnitude of the generated tension. We ran simulations at a fixed actin density, filament length, and number of myosin motors for a range of seeding thickness values ( $h_0 = 103$  nm to 412 nm, Supplementary Fig. 5f). The density was fixed by setting the number of filaments to  $N_f = \beta h_0$  with  $\beta = 11.37$  nm<sup>-1</sup>, to match the density in the original simulations. All simulations were run with  $l_a = 500$  nm. We find that the tension is weakly dependent on the seeding thickness, but does not exhibit a maximum tension at intermediate seeding thicknesses (Supplementary Fig. 5f).

### Changing filament length at fixed seeding thickness

We then tested for the effect of filament length on tension generation when the total amount (total length) of actin  $L_a = N_f l_a$  and the seeding thickness  $h_0$  are kept constant (Supplementary Fig. 5g). We ran simulations where the filament length was varied over the range 200 nm to 800 nm, similar to the range explored in Fig. 4d. The number of the filaments  $N_f$  was set to the closest integer to  $L_a/l_a$  with  $L_a = 693.75$   $\mu\text{m}$ , the seeding thickness was set to  $h_0 = 250$  nm, and the crosslinker binding probability was changed to  $p_x = 0.5$ , to account for a decrease in actin density relative to the simulations displayed in Fig. 4d. The results show that filament length still modulates tension, with a peak at intermediate filament lengths (Supplementary Fig. 5g).

## Discussion of model assumptions

We briefly discuss here some of the model assumptions.

### Discussion of myosin stall force and kinetics

Myosin minifilaments represent filaments of myosin II motors. Individual myosin II motors have been shown to produce between 2 and 5 pN of force (2). Individual motors are not processive, but have been shown to assemble into minifilaments of 10 to 30 motors *in vitro* (3) and in the lamellipodium of fibroblasts (4). Based on this evidence, it is expected that myosin motors behave collectively as an ensemble of motors (5). In our simulations, we chose for simplicity a linear force-velocity relationship describing the effective behaviour of one minifilament. We also have set the minifilament stall force to a value of 40 pN, as previously estimated based on the assumption that there are about 20 myosin motors per minifilament, with individual motors producing an average of 2 pN while working in the ensemble (6).

### Discussion of the assumption of rigid rods

For simplicity, we took actin filaments to be straight rods in our simulations, assuming that the distance between crosslinkers is sufficiently small or the filament bending rigidity sufficiently high. We discuss here this assumption. Note that calculating the bending of filaments in a crosslinked network is a complex problem and we only intend here to estimate rough orders of magnitudes.

An estimate of the average distance between crosslinkers,  $d_x$ , in simulated networks can be obtained by taking the total length of actin and dividing by twice the total number of crosslinkers,  $N_x$ :

$$d_x = \frac{N_f l_a}{2N_x}. \quad (14)$$

The value of  $d_x$  calculated from simulations depends on the length of filaments. With filament lengths  $l_a$  taken between 200 nm to 800 nm, we take from simulations  $N_x \sim 8000$  for the lowest filament length and  $N_x \sim 21000$  for the largest filament length, and therefore  $30 \text{ nm} < d_x < 60 \text{ nm}$ . This characteristic distance between crosslinking points is small when compared to the persistence length of actin filaments,  $\sim 10 \mu\text{m}$ .

To give an order of magnitude of how much filaments could bend if the filament bending rigidity was taken into account, we first calculate the deformation induced by a normal force acting on a portion of filament between two crosslinkers. For simplicity we consider here a filament between two crosslinking points as a simply supported beam of length  $L$ , subjected to a force  $F$  acting in the middle of the filament. The deflection can then be written:

$$w = \frac{FL^3}{48\kappa}, \quad (15)$$

where  $\kappa$  is the actin filament flexural rigidity that can be calculated from the actin persistence length  $l_p \simeq 10 \mu\text{m}$  (11),  $\kappa = l_p k_b T \simeq 4.1 \times 10^{-26} \text{ N m}^2$ . Using  $L=60 \text{ nm}$  a characteristic

distance between crosslinking points and taking  $F = f_0 = 40$  pN the force exerted by one myosin minifilament, we calculate a deflection  $w$  of about  $\sim 4$  nm, small compared to the length of actin filaments and to the distance between cross linkers (see above).

One can also estimate the buckling threshold for one filament that would result from an axial load along the filament. To consider this we use the Euler buckling equation,

$$F^* = \frac{\pi^2 \kappa}{(KL)^2}. \quad (16)$$

where  $F^*$  is the critical applied load tangential to the filament,  $K$  is the column effective length factor which depends on boundary conditions applied on the filament and take values between 0.5 and 2, and  $L$  is the length at which the beam becomes unstable. Imposing  $F^*$  to be equal to the force exerted by one myosin minifilament  $f_0 = 40$  pN, we find a critical length  $L$  for actin filaments to undergo a buckling instability between 50 nm and 200 nm. Again considering here for simplicity that the filament is fixed at its crosslinking positions, this shows that the largest mean distance between crosslinkers is at the lower limit of buckling lengths, suggesting that buckling under axial loads imposed by myosin minifilaments is unlikely to be a frequent event in our simulations. In general, crosslinkers are not rigidly fixed in a network and the network behaviour thus likely to be more complex than considered here.

While filament bending, in principle, could occur in the actin cortex, our simulations indicate that taking filament bending into account is not necessary to generate tension, as has been shown in previous studies (7, 8). In addition to exhibiting contractility, our simulated actomyosin networks produce a non-monotonic relationship between tension and filament length. Including filament bending in simulations would be interesting but would require imposing a value for the filament bending rigidity, which can be influenced by a number of factors, including: bundling of actin filaments (9), actin binding proteins (e.g. tropomyosin (10), cofilin (11)) or the nucleotide state (ATP or ADP-bound) of monomers in the filaments (12). For all these reasons, we chose not to include bending in our model. Interestingly, several previous studies have proposed that filament bending under compression could be a mechanism accounting for cortical tension generation in actomyosin networks (see Discussion in Main Text and references 13-15). In our model, tension generation is achieved without this effect and results from asymmetries in actin network response to myosin stresses (Fig. 5). It will be interesting in the future, to investigate the influence of filament bending on tension generation in our model.

## Additional References

1. Svitkina, T. M., Verkhovsky, A. B., and Borisy, G. G. Improved procedures for electron microscopic visualization of the cytoskeleton of cultured cells. *J. Struct. Biol.* **115**, 290–303 (1995).
2. Finer, J. T., Simmons, R. M., Spudich, J. A., et al. Single myosin molecule mechanics: piconewton forces and nanometre steps. *Nature* **368**(6467), 113–119 (1994).
3. Niederman, R. and Pollard, T. D. Human platelet myosin II. In vitro assembly and structure of myosin filaments. *J. Cell Biol.* **67**(1), 72–92 (1975).

4. Verkhovsky, A. B. and Borisy, G. G. Non-sarcomeric mode of myosin II organization in the fibroblast lamellum. *J. Cell Biol.* **123**(3), 637–652 (1993).
5. Erdmann, T. and Schwarz, U. S. Stochastic force generation by small ensembles of myosin II motors. *Phys. Rev. Lett.* **108**(18), 188101 (2012).
6. Nie, W., Wei, M.-T., Ou-Yang, H. D., Jedlicka, S. S., and Vavylonis, D. Formation of contractile networks and fibers in the medial cell cortex through myosin-II turnover, contraction, and stress-stabilization. *Cytoskeleton* **72**(1), 29–46 (2015).
7. Carlsson, A. E. Contractile stress generation by actomyosin gels. *Phys. Rev. E* **74**(5), 051912 (2006).
8. Hiraiwa, T. and Salbreux, G. Role of turnover in active stress generation in a filament network. *Phys. Rev. Lett.* **116**(18), 188101 (2016).
9. Claessens, M. M. A. E., Bathe, M., Frey, E., and Bausch, A. R. Actin-binding proteins sensitively mediate f-actin bundle stiffness. *Nat. Mater.* **5**(9), 748–753, 09 (2006).
10. Kojima, H., Ishijima, A., and Yanagida, T. Direct measurement of stiffness of single actin filaments with and without tropomyosin by *in vitro* nanomanipulation. *Proc. Natl. Acad. Sci. U.S.A.* **91**(26), 12962–12966 (1994).
11. McCullough, B. R., Blanchoin, L., Martiel, J.-L., and Enrique, M. Cofilin increases the bending flexibility of actin filaments: implications for severing and cell mechanics. *J. Mol. Biol.* **381**(3), 550–558 (2008).
12. Isambert, H., Venier, P., Maggs, A., Fattoum, A., Kassab, R., Pantaloni, D., and Carlier, M. Flexibility of actin filaments derived from thermal fluctuations. effect of bound nucleotide, phalloidin, and muscle regulatory proteins. *J. Biol. Chem.* **270**(19), 11437–11444 (1995).
13. Soares e Silva, M., Depken, M., Stuurmann, B., Korstena, M., MacKintosh, F. C. Active multistage coarsening of actin networks driven by myosin motors. *Proc. Natl. Acad. Sci. USA* **108**, 9408–9413 (2011).
14. Lenz, M., Thoresen, T., Gardel, M. L. and Dinner, A. R. Contractile units in disordered actomyosin bundles arise from F-actin buckling. *Phys. Rev. Lett.* **108**, 238107 (2012).
15. Murrell, M. P. and Gardel, M. L. F-actin buckling coordinates contractility and severing in a biomimetic actomyosin cortex. *Proc. Natl. Acad. Sci. USA* **109**, 20820–20825 (2012).
16. Clark, A. G. *Thickness, dynamics and mechanics of the actomyosin cortex*. PhD thesis, Technische Universität Dresden, Dresden, Germany, (2013).
17. Machicoane, M., de Frutos, C. A., Fink, J., Rocancourt, M., Lombardi, Y., Garel, S., Piel, M., and Echard, A. Slk-dependent activation of ERMs controls LGN–NuMA localization and spindle orientation. *J. Cell Biol.* **205**(6), 791–799, 06 (2014).
18. Estey, M. P., Di Ciano-Oliveira, C., Froese, C. D., Bejide, M. T., and Trimble, W. S. Distinct roles of septins in cytokinesis: Sept9 mediates midbody abscission. *J. Cell Biol.* **191**(4), 741–749, 11 (2010).